Study on heat capacity of doped UO_2

Yuji ARITA

Contents

1. Introduction

1.1. Heat capacity of fluorite structured compounds

Fluorite structured compounds (CaF_2, PbF_2, $SrCl_2$, etc.) provide one of the simplest systems to study the phenomena of superionic transition [1-3]. As seen from Fig. 1-1, those transition temperatures were almost $0.8Tm$ (Tm : melting point). An origin of this transition was regarded to be due to partial disorder of anion (cation for anti-fluorite structure) sublattice [7,8]. From studies by neutron scattering [9], anion conductivity [10,11] and diffusion coefficient [12,13], the phase transition was found to involve the generation of anion interstitial disorder. This phenomenon was also called as a partial melting of the anion sublattice.

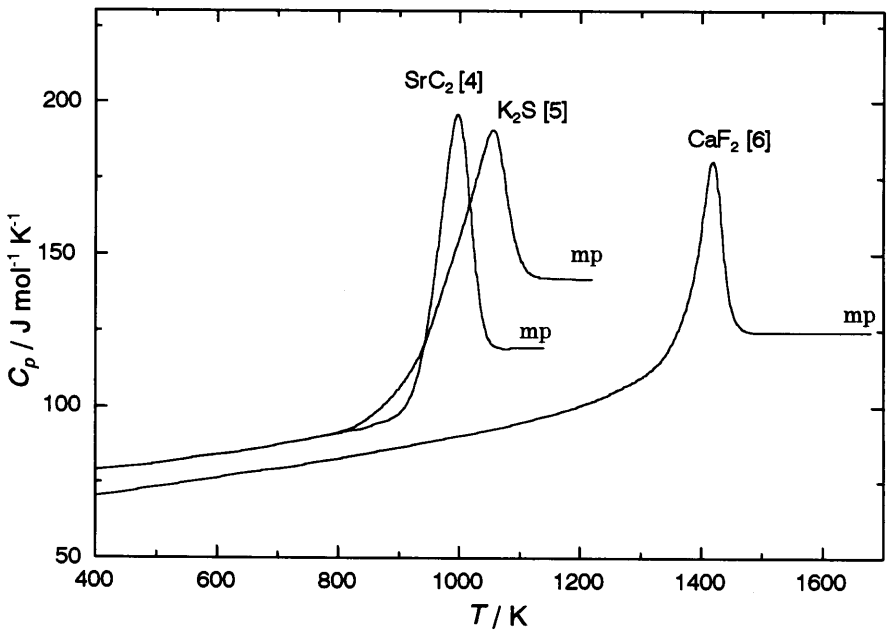

Fig. 1-1 Anomaly in heat capacity (lambda transition) of fluorite and anti-fluorite type of compounds.

1.2. Heat capacity of undoped UO_2

The heat capacity of UO_2 is one of the most important properties of nuclear fuel materials to evaluate their thermal properties under irradiation in a nuclear reactor.

An anomalous increase in the heat capacity of undoped UO_2 at high temperature above 1600 K has attracted the attention of many researchers and an origin of this increase has been the subject of discussions for many years.

Some representative results [14-20] of high temperature heat capacity measurements of undoped UO_2 reported so far are shown in Fig. 1-2. Below about 1000 K, the heat capacity data obtained by Grönvold et al. [14] by adiabatic calorimetry are known as the most reliable ones. Most of the heat capacity data above 1000 K were obtained by drop calorimetry. The drop calorimetry is the indirect method; from which enthalpy data are obtained, then heat capacity is calculated by differentiating them with respect to temperature. In Fig. 1-2, the data by Hein et al. [17] and Kerrisk and Clifton [20], both of which were the same data obtained by the drop calorimetry, become different with each other due to use of different equations for fitting the data. As seen from these data, the heat capacity of UO_2 rises remarkably above about 1600 K. The origin of this anomalous rise of heat capacity of UO_2 has become the subject of the discussions by many investigators.

Szwarc [19] first analyzed this excess heat capacity as a contribution of formation of oxygen Frenkel defects with the formation energy (ΔH_f) of 3.11 eV. Kerrisk and Clifton [20] made a similar analysis based on their own data and obtained the formation energy of 3.28 eV. Although these analysis fitted well to the experimental heat capacity curve, the values of the ΔH_f were not in good agreement with the value of about 5 eV theoretically evaluated by Harding et al.[21] and Jackson et al. [22].

Catlow [23] and Thorn et al. [24] suggested the contribution due to electron-hole pair formation in UO_2 to the excess heat capacity at high temperatures:

$$2U^{4+} \rightarrow U^{5+} + U^{3+}. \qquad (1)$$

The formation energy for electron-hole pairs was found from calculation by Harding et al. [21] to be about 1.7 eV. Browning [25] reanalyzed the heat capacity data of Szwarc [19] and Kerrisk and Clifton [20] and obtained the formation energy for electron-hole pairs of about 1.71 eV, which is in good agreement with the theoretically evaluated value of about 1.7 eV [21]. He concluded that the excess heat capacity of UO_2 at high temperatures is the contribution due to the electron-hole pair formation. However, there are some confusions in the definition of the formation energy of defects in his paper, and the experimental value he obtained, 1.71 eV, should be doubled for comparing with the calculated value.

From the different analysis of the enthalpy data by Kerrisk and Clifton [20], Bredig [26] first pointed out the existence of a lambda type order-disorder transition of oxygen sublattice in the heat capacity of UO_2 at 2670 K (he called as "Bredig transition"), which was regarded as the same origin as that for halide with fluorite structure i.e. the partial melting of oxygen sublattice. The existence of Bredig transition has been discussed since then, but the appearance of the lambda type change in the heat capacity curve is very dependent on how to differentiate the enthalpy data with temperature. Recently, Ralph and Hyland [27] applied the quasi-local linear regression (QLLR) method, more acceptable method for the differentiation of the enthalpy data, to the enthalpy data by Hein et al. [17], and the results are also shown in Fig. 1-2 (shown with error bars). A pronounced heat capacity peak at 2610 K was revealed by this method as predicted by Bredig, and also a nearly constant heat capacity after the transition was

characterized as seen from Fig. 1-2.

In addition to these heat capacity measurements or analysis, Hutchings et al. [28,29] reported the occurrence of appreciable oxygen Frenkel disorder above 2000 K by neutron diffraction and diffuse scattering, which is thought to be the first direct evidence of the thermal excitation of Frenkel defects in the oxygen sublattice in UO_2. These facts support the existence of Frenkel disorder at high temperatures and the occurrence of Bredig transition below the melting point of UO_2.

Several microscopic models [30-35] were proposed to describe theoretically the structural transition to the superionic state of fluorites, and were later generalized for the description of the oxides with the same atomic structure [36]. These models describe the distribution of the Frenkel defects in both sublattices accounting for their far distance interaction.

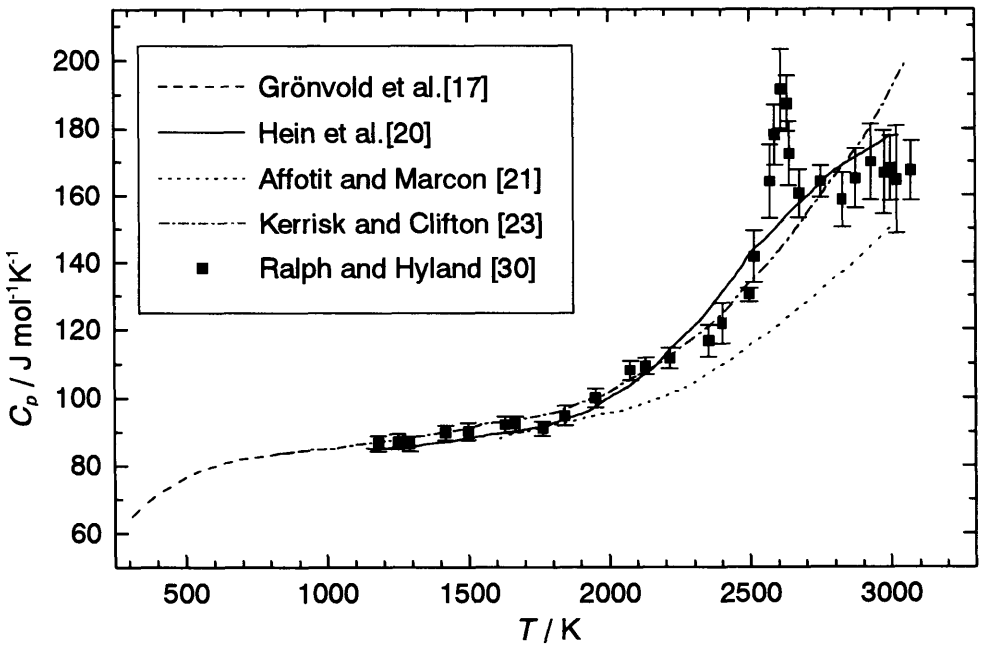

Fig. 1-2 Heat capacity of UO_2.

1.3. Purpose of this study

It is the aim of this study to investigate whether there is an anomalous heat capacity originated from oxygen Frenkel defects in undoped UO_2, of which transition (onset) temperature is so high that direct methods of heat capacity measurement are not applicable. Therefore, in this study, the heat capacity of doped UO_2 were measured. By doping the aliovalent cation, the concentration of oxygen Frenkel defect will increase to keep the electroneutrality and thus the onset temperature of excess heat capacity was considered to become lower than that of undoped UO_2. Furthermore, we improved a calorimeter to expand the upper limit of temperature for heat capacity measurement. In addition to the heat capacity measurement, EXAFS (Extended X-ray Absorption Fine Structure) measurement was also performed to clarify microstructural change of anion (oxygen) sublattice.

In nuclear engineering, the heat capacities and other thermal functions are the important properties to evaluate thermal properties of advanced nuclear fuel or irradiated nuclear fuel in nuclear reactor.

References

[1] *"The Chemistry of Extended Defects in Non-Metallic Solids"*, ed. L.Eyring and M.O'Keefe (North-Holland, Amsterdam, 1970).

[2] *"Fast Ions Transport in Solids"*, ed. W.van Gool (North-Holland, Amsterdam, 1973).

[3] Yu.Ya.Gurevich and Yu.I.Kharkatz, *Phys. Rep.*, **139** (1986) 201.

[4] A.S.Dworkin and M.A.Bredig, *J. Chem. Eng. Date.*, **8** (1963) 416.

[5] A.S.Dworkin and M.A.Bredig, *J. Phys. Chem.*, **72** (1968) 1277.

[6] B.F.Naylor, *J. Am. Chem. Soc.*, **64** (1945) 150.

[7] M.Dixon and M.J.Gillan, *J. Phys. C : Solid State Phys.*, **11** (1978) 165.

[8] C.R.A.Catlow, J.D.Comins, F.A.Germano, R.T.Harley and W.Hayes, *J. Phys. C : Solid State Phys.*, **11** (1978) 3197.

[9] M.H.Dickens, W.Hayes, C.Smith and M.T.Hutchings, *J. Phys. C : Solid State Phys.*, **15** (1982) 4043.

[10] H.Matzke, *J. Mater. Sci.*, **5** (1970) 831.

[11] M.Beniere, M.Chemla and F.Beniere, *J. Phys. Chem. Solids*, **40** (1979) 729.

[12] V.M.Carr, A.V.Chadwick and R.Saghafian, *J. Phys. C : Solid State Phys.*, **11** (1978) L637.

[13] D.Glasser-Leme and H.Matzke, *Solid State Commun.*, **3** (1982) 201.

[14] F.Grönvold, N.J.Kveseth, A.Sveen and J.Tichy, *J. Chem. Thermodyn.*, **2** (1970) 665.

[15] D.R.Fredrickson and M.G.Chasanov, *J. Chem. Thermodyn.*, **2** (1970) 623.

[16] A.E.Ogard and J.A.Leary, *"Symposium of Thermodynamics of Nuclear Materials"*, IAEA, Vienna, (1967).

[17] R.A.Hein, P.N.Flagella and J.B.Conway, *J. Am. Ceram. Soc.*, **51** (1968) 291.; R.A.Hein, L.H.Sjodahl and R.Szwarc, *J. Nucl. Mater.*, **25** (1968) 99.

[18] C.Affortit and J.P.Marcon, *Rev. Int. Hautes Temper.Refract.*, **7** (1970) 236.

[19] R.Szwarc, *J. Phys. Chem. Solids*, **30** (1969) 705.

[20] J.F.Kerrisk and D.G.Clifton, *Nucl. Technol.*, **16** (1972) 531.

[21] J.H.Harding, P.Masri and A.M.Stoneham, *J. Nucl. Mater.*, **92** (1980) 73.

[22] R.A.Jackson, C.Richard, A.Catlow and D.Murray, *J. Chem. Soc. Faraday Trans.*2, **83** (1987) 1171.

[23] C.R.A.Catlow, *Proc. Roy. Soc. (London)* **A353** (1977) 533.

[24] R.J.Thorn, G.Winslow and J.S.Zeomek, *J. Nucl. Mater.*, **87** (1979) 416.

[25] P.Browning, *J. Nucl. Mater.*, **98** (19 81) 345.

[26] M.A.Bredig, *Colloq. Int. C.N.R.S.*, (**205**) (1971) 183.

[27] J.Ralph and G.J.Hyland, *J. Nucl. Mater.*, **132** (1985) 76.

[28] M.T.Hutchings, K.Clausen, W.Hayes, J.E.Macdonald, R.Osborn and P.Schnable, *High Temp. Sci.*, **20** (1985) 97.

[29] M.T.Hutchings, *J. Chem. Soc. Faraday Trans.*2, **83** (1987) 1253.

[30] M.J.Rice, S.Strassler and G.A.Toombs, *Phys. Rev. Lett.*, **32** (1974) 596.

[31] B.A.Huberman, *Phys. Rev. Lett.*, **32** (1974) 1000.

[32] D.O.Welch and G.J.Dienes, *J. Phys. Chem. Solids*, **38** (1977) 311.

[33] J.Oberschmidt, *Phys. Rev.*, **B23** (1981) 5038.

[34] N.H.March, D.D.Richardson and M.P.Tosi, *Solid State Commun.*, **35** (1980) 903.

[35] M.S.Veshchunov, *J. Nucl. Mater.*, **188** (1992) 189.

[36] S.W.Tam, J.K.Fink and L.Leibowitz, *J. Nucl. Mater.*, **130** (1985) 199.

2. Improvement of DHPC (Direct Heating Pulse Calorimeter)

2.1. Introduction

Measurements of the high-temperature heat capacity of non-metallic materials have been carried out mostly by the drop method. In this method, the enthalpy is directly measured and the heat capacity is calculated by differentiating the enthalpy with respect to temperature; a somewhat large error may arise when the sample has a phase transition since the high-temperature phase is apt to be quenched and the temperature dependence for the enthalpy data around phase transition is not precisely determined. For the direct determination of heat capacity C_p, measurement of the thermal energy Q given to the sample and the temperature rise ΔT_S of the sample are required :

$$C_p = \frac{Q}{\Delta T_S} . \tag{1}$$

At high temperatures it can be assumed that the heat leak q from the sample to its surroundings is mainly due to radiation, and that ΔT_S is much smaller than the sample temperature, T_S, then :

$$q \propto S \cdot \Delta T_m \cdot \Delta t \cdot T_S{}^3 , \tag{2}$$

where S is the area of the sample surface, ΔT_m the mean temperature difference between the sample and surroundings, and Δt the time required for the measurement. Therefore, the relative error δ is written as

$$\delta = \frac{q}{Q} \propto \frac{S}{C_p} \frac{\Delta T_m}{\Delta T_S} \Delta t \cdot T_S{}^3 . \tag{3}$$

For an adiabatic calorimeter Δt becomes large because of slow transmission of heat from heater to sample, so it is necessary to keep $\Delta T_m / \Delta T_S$ as small as possible by

precise adiabatic control to reduce the relative error. However, δ becomes larger in proportion to T_S^3 at higher temperatures, because ΔT_m is obtained as a limiting value as a result of the adiabatic control. The measurement of heat capacity for non-metallic samples using the adiabatic calorimeter has been reported at temperatures up to about 1000 or 1100 K [1,2], which is considered to be the limiting temperature with use of this type of calorimeter for non-metallic samples.

For the measurement above 1000 K, it is required to reduce Δt. Two high-speed heating methods, the laser flash method and the direct heating pulse method, are known. In the former method [3,4], a pulse of laser radiation impinges on the front surface of the sample in the form of a disc pellet, and it takes some time until a temperature distribution becomes uniform over the whole sample. If the thermal diffusivity of the sample is small, Δt is frequently over 10 s. Although thin sample is desirable in order to reduce Δt, δ cannot always be reduced since S/C_p increases. In the latter method, although the sample is limited to electrically conducting materials of uniform rod shape, the sample is heated uniformly and Δt can be sufficiently reduced within the response time of the thermometer. As the direct heating pulse calorimetry, two methods, the continuous heating method and the intermittent heating method, are known. The continuous heating method at a high heating rate of 10^2 - 10^7 K s^{-1} has been used for metallic samples [5-10]. For semiconducting samples a wire heating method has been used by Affortit and co-workers [11-13], who measured heat capacities of UO_2, UC, UN and $U_{1-X}Pu_XO_2$. However, there are some difficulties in the use of the continuous heating method in the measurement of semiconducting samples. The first difficulty is to obtain a high heating rate, because the heating of less conductive materials with a high heating rate needs a high-voltage power supply. The second is the difficulty

of establishing a uniform temperature distribution in the radial direction of the sample, which causes a large temperature gradient in this direction by heat flow from the surface of the sample to the surroundings.

Intermittent (pulse) heating method developed much earlier [14,15] has been used to measure the heat capacity of metallic samples at low heating rate. The calorimeter reported by Pallister [15] was used to measure the heat capacity of iron up to 1520 K with an inaccuracy of within 2%. In his apparatus, a semi-adiabatic shield enclosing the sample was provided for reducing the heat leak. The shield consisted of the same material and had the same cross-section as the sample.

Naito et al.[16] developed a intermittent (pulse) heating method with an adiabatic shield to measure the heat capacity of semiconducting materials up to 1500 K, and they called their instrument as a " direct heating pulse calorimeter ".

2.2. Direct heating pulse calorimeter

A direct heating pulse calorimeter (DHPC) was designed and constructed for measuring the heat capacity of semiconducting materials at high temperatures [16]. This method is one of the pulse heating calorimetry. In this calorimeter a sample was heated directly by pulse current. Figures 2-1 and 2-2 show a block diagram and the central part of the apparatus, respectively. In this calorimeter a cylindrical sample rod is connected to the stainless steel electrodes with the molybdenum holders. Platinum film is placed between sample and holder to reduce the contact resistance. Double cylindrical molybdenum plate was used as an adiabatic shield enclosing a sample. At first the sample is maintained at an equilibrium constant temperature by an external heater. Electrical energy is then supplied simultaneously to the sample and shield by

pulse heating. The power supply is variable to control the temperature rise (ΔT_S) of the sample. The power for the shield is adjusted to produce the same temperature rise (ΔT_{sh}) as for the sample. The duration of pulse heating is controlled from 0.25 to 2.0 s by a circuit using a silicon-controlled rectifier switch for low voltages and a high speed relay for high voltages. The temperature rises ΔT_S and ΔT_{sh} are usually chosen to be between 1 and 4 K.

The temperature rise of the sample is measured by a R-type (Pt/Pt13%Rh) thermocouple of 0.15 mm diameter, which is contacted on the surface of the sample with zirconia cement in order to obtain a good thermal contact and a sufficient electrical insulation between the sample and the thermocouple. The temperature rise of the shield is also measured by a R-type thermocouple of 0.2 mm diameter welded on the molybdenum shield. The voltage drop in the sample is measured by two wires of

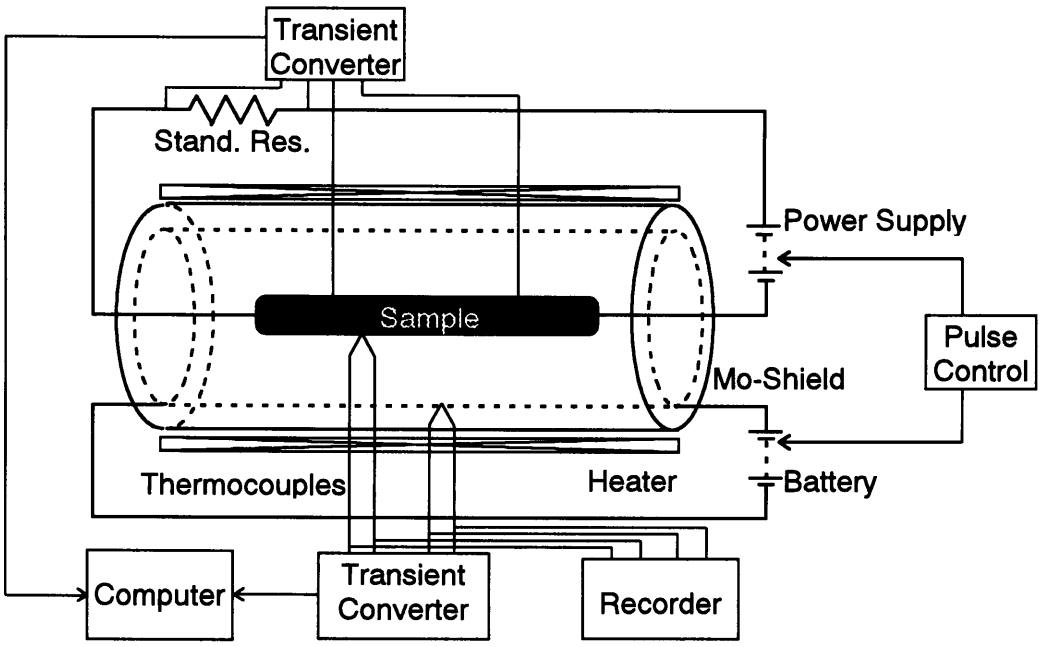

Fig. 2-1 Block diagram of the apparatus.

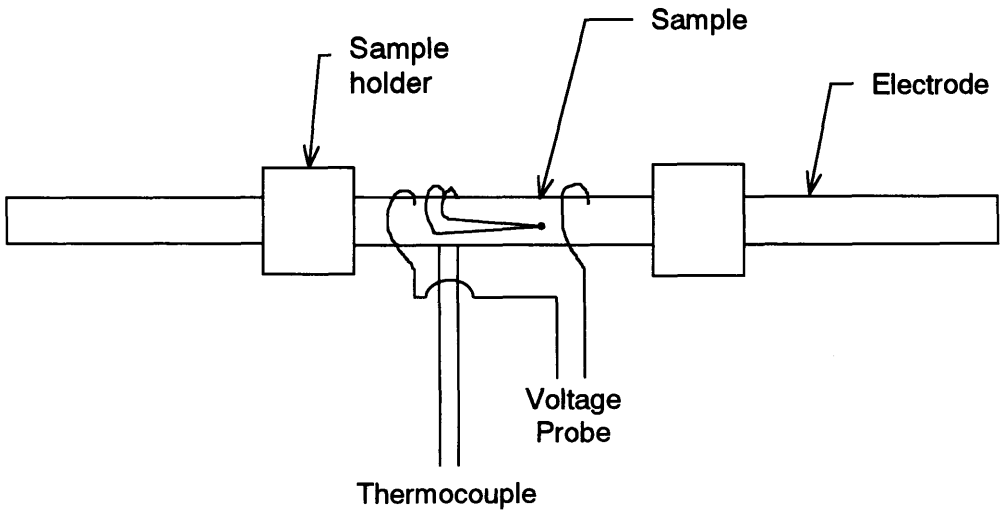

Fig. 2-2 The central part of the apparatus.

Pt13%Rh inserted into the sample at an interval of about 30 mm. The sample, the shield, the external heater and an alumina furnace are placed in an evacuated stainless steel bell-jar.

2.3. Samples

The samples whose dimensions are 5-10 mm in diameter and 50-80mm in length were used for DHPC in this study. In the calorimeter the sample was connected to stainless steel tube electrodes with a molybdenum holder.

2.4. Procedure

The calorimeter is maintained at a constant equilibrium temperature by an external heater, then electrical energy is supplied to a sample and the two shields simultaneously by pulse currents. The heat capacity of the sample is calculated from eq.(4):

$$C_p = \frac{M}{m}\frac{Q}{\Delta T_S}, \qquad (4)$$

where $m=(l/l_0)m_0\gamma$ and $Q=(V_1V_2/R)\Delta t$. M represents the molecular weight of the sample, m the effective mass of the sample, m_0 the total mass of the sample, l the effective length of the sample (the distance between voltage probes), l_0 the total length of the sample, V_1 the voltage drop between voltage probes, V_2 the voltage drop of a standard resistance, R the standard resistance, Δt the heating period and γ the correction factor for uniformity of the sample.

2.5. Details of the improvement

In the case of the heat capacity measurements of doped UO_2 by DHPC there were some limitations : ① a maximum temperature for the heat capacity measurements was about 1300 K, ② a capacity of power supply was too small to load a sufficient current into the high resistant sample and ③ a pulse controller composed of complex electric circuit did not produce a reproducible pulse duration time and its repair was rather troublesome. Improvements for elimination of these limitation made in this study for reliable heat capacity measurements are shown in following sections.

2.5.1. Expansion of measurable temperature range

Since an onset temperature at which heat capacity increases anomalously is regarded to be above 1600 K, it is desirable to expand the measurable temperature range up to 1600 K. The limitation was mainly caused by the snapping of a heating wire. The reasons of the snapping were a reaction between Pt30%Rh wire and Si which is included as an impurity in the alumina insulator, a thinning of the wire by

vaporization and a partial overheat by a recrystallization of the Pt30%Rh alloy.

At first, we tried to use a tungsten wire as a heater because of its high melting point (3673 K), however, the tungsten wire had snapped soon. Since an oxygen partial pressure in a vacuum vessel was about 10^{-1} Pa, the tungsten can be easily oxidized. It was difficult and expensive to decrease the oxygen partial pressure in the vessel. Thus we gave up this idea.

Next, to decrease the effects of vaporization and recrystallization a diameter of the heating wire was made thick from 0.5 mm to 0.7 mm in diameter. Further the reaction of heater with Si was restrained by using pure alumina insulator. After those improvements we could measure heat capacities up to 1550 K for regular usage and 1783 K in maximum. Since a melting point of stainless steel which was used for electrode is 1673 K, a molybdenum electrode was used above 1600 K.

2.5.2. Improvement for insulating (or semiconducting) materials

In the case of doped UO_2 the resistance was $10^4 \sim 10^7\ \Omega$ at room temperature. Since the maximum voltage of the power supply for the sample was 180 V, the temperature rise of the sample was smaller than 0.5 K for the sample with $10^7\ \Omega$ resistance. This problem was solved by using the power supply whose capacity is 550 V. But another problem should be considered. An isolation amplifier connected to voltage probes had $10^7\ \Omega$ itself as internal impedance. It means that almost equal current will flow through the amplifier and the sample. Therefore the temperature rise will be half of essential one. To decrease the current loss to the amplifier, we changed the amplifier which has high internal impedance of $10^{10}\ \Omega$.

2.5.3. Improvement of pulse controller

The pulse controller previously used was constructed with a delay circuit composed of about hundred electrical parts and was often missed to generate the pulse. Therefore, a new pulse controller was planned. A circuit diagram is shown in Fig. 2-3, which is a simple sequential circuit with only two timers and two relays. With the new pulse controller no pulse control miss occurred.

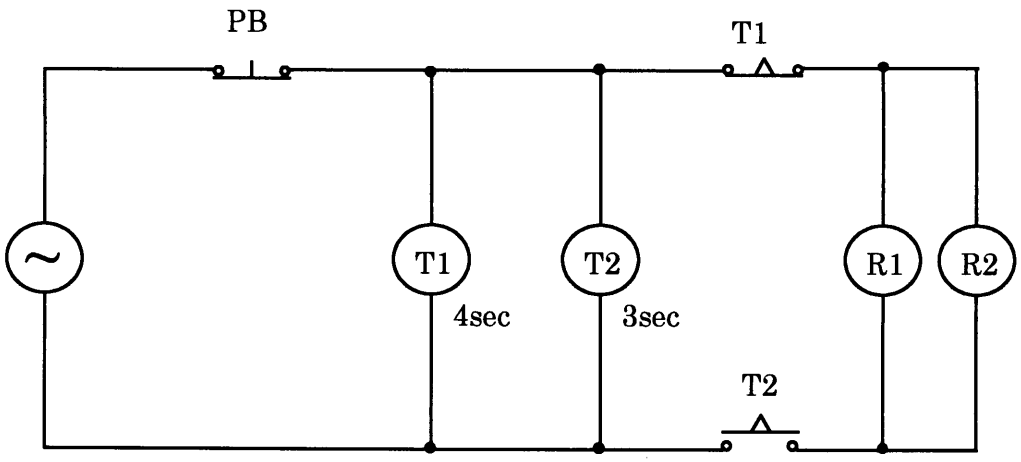

T : timer, R : relay
PB : pushed switch

Fig. 2-3 Diagram of pulse timing circuit.

References

[1] F.Grönvold, *Acta. Chem. Scand.*, **21** (1967) 1695.

[2] K.Naito, H.Inaba, M.Ishida, Y.Saito and H.Arima, *J. Phys. E. Sci. Instrum.*, **7** (1974) 464.

[3] W.J.Park, R.J.Jenkins, C.P.Butler and G.L.Abbutt, *J. Appl. Phys.*, **32** (1960) 2679.

[4] Y.Takahashi, *J. Nucl. Mater.*, **51** (1974) 17.

[5] T.E.Pochapsky, *Rev. Sci. Instrum.*, **25** (1954) 238.

[6] D.C.Wallace, *J. Appl. Phys.*, **31** (1960) 168.

[7] T.G.Kollie, *Rev. Sci. Instrum.*, **38** (1967) 1452.

[8] A.Cezairliyan, M.S.Morse, H.A.Berman and C.W.Beckett, *J. Res. NBS*, **A74** (1970) 65.

[9] I.Ya.Dikhter and S.V.Levedev, *High Temp.- High Press.*, **2** (1970) 55.

[10] R.E.Taylar, *High Temp.- High Press.*, **4** (1972) 523.

[11] C.Affortit, *High Temp.- High Press.*, **1** (1969) 27.

[12] C.Affortit and J.C.Boivineau, *BIST Commissariat a l'Energie Atomique* No.**180** Aviril (1973) 52.

[13] C.Affortit and R.Lallement, *Revue. Int. Hautes Temp. Refrac.*, **5** (1968) 19.

[14] E.Lapp, *Ann. Phys., Paris* **12** (1929) 442.

[15] P.R.Pallister, *J. Iron Steel Inst.*, **161** (1949) 87.

[16] K.Naito, H.Inaba, M.Ishida and K.Seta, *J. Phys. E. Sci. Instrum.*, **12** (1979) 712.

3. Heat capacity of doped UO_2

3.1. Introduction

It has been reported that a small amount of aliovalent cations such as Ti, Nb, La etc., added to UO_2 can improve mechanical properties and irradiation behavior to attain high burnup [1], and that many fission products (FP) solve into UO_2 matrix under high burnup condition. Transuranium elements (TRU), which have long radioactive half life such as americium, curium and neptunium, have been recently planned to be burnt out in a nuclear reactor in the form of solid solution with UO_2.

Hence thermodynamic properties of UO_2 doped with aliovalent cations, FP and TRU are of importance to understand the stabilities of the fuels in the reactor. Although the heat capacity is one of the useful properties to calculate the thermodynamic quantities, little is measured the heat capacity for doped UO_2.

The heat capacities of gadolinia-doped UO_2 ($U_{1-y}Gd_yO_{2.0}$, y = 0.044, 0.073, 0.101, 0.142) have been recently measured from room temperature to 1500 K in the present author's laboratory [2,3], and an anomalous increase in the heat capacity of each sample was first observed at high temperatures from about 700 K for y = 0.142 to 1200 K for y = 0.044. The anomalous increase in the heat capacity of undoped UO_2 above 1500 K was interpreted as due to formation of the Frenkel pairs of oxygen by several investigators [4,5] and reviewed by Naito [6].

In this study the heat capacities of $U_{1-y}M_yO_{2-X}$ (M : di-, tri-, tetra- and penta-valent cation) were measured from 300 to 1550 K by direct heating pulse calorimetry to clarify the origin of an anomalous increase in the heat capacity of doped and undoped UO_2.

3.2. Experimental

3.2.1. Sample preparation

The mixture of MO_x (M = dopant cation) and UO_2 powder was shaped into a cylindrical rod of about 6 mm in diameter and 60 mm in length using an evacuated rubber press with a hydrostatic pressure of about 400 MPa. The cylindrical rod was sintered and homogenized at 1673 K for 7 days. This sintering and homogenizing process was repeated several times, and then the samples were annealed under the conditions shown in Table 3-1 so as to obtain the stoichiometric composition (O/M = 2.00) or hypo-stoichiometric composition according to the thermogravimetric study [7-18]. X-ray diffraction analysis indicated that each sample rod was a single phase.

Table 3-1. The annealing conditions of sample after sintering (and homogenizing)

Dopants	Valence	Annealing condition	Ref.
La	+3	At 1323 K for 2 days in H_2 flow	[7]
Nd	+3	At 1273 K for 2 days in H_2 flow	[8]
Y	+3	At 1323 K for 1 day in H_2 flow	[9]
Sc	+3	At 1323 K for 1 day in H_2 flow	[10]
Mg	+2	At 1673 K for 7 days in Ar flow : for O/M = 2.0	[11]
		At 1273 K for 2 days in H_2 flow : for O/M < 2.0	[12]
FP	+2~+4	At 1273 K for 1 day in H_2 flow	[13]
Ti	+4	At 1323 K for 2 days in H_2 flow	[14]
Ce	+4	At 1273 K for 1 day in H_2 flow	[15]
Zr	+4	At 1273 K for 1 day in H_2 flow	[16]
Pr	+3 or +4	At 1273 K for 1 day in H_2 flow	[17]
Nb	+5	At 1323 K for 2 days in H_2 flow	[18]

3.2.2 Heat capacity measurement

As described in section 2, heat capacities and electrical conductivities were measured simultaneously by the direct heating pulse calorimeter. The electrical conductivity was determined from a current passing through the standard resistance and a voltage drop between voltage probes.

The heat capacities and the electrical conductivities were measured in the temperature range from room temperature to about 1500 K.

3.3. Results and discussion

3.3.1. Heat capacity of undoped UO_{2+x}

At first the heat capacity of undoped $UO_{2.0}$ was measured to examine the reliability and an accuracy of the apparatus. In Fig. 3-1 the result is shown in comparison with the reference data of $UO_{2.0}$ measured by Grönvold et al.[19] and Fredrickson and Chasanov [20]. Our result was in good agreement with the reference data in all temperature range. The equation for the heat capacity of $UO_{2.0}$ in this study was given by the least-squares method as :

$$C_p / \mathrm{J\ mol^{-1}\ K^{-1}} = 67.399 + 1.2288 \times 10^{-2} (T/\mathrm{K}) + 8.6448 \times 10^{3} (T/\mathrm{K})^{-1} - 3.5393 \times 10^{6} (T/\mathrm{K})^{-2}, \quad (297 < T/\mathrm{K} < 1550). \qquad (1)$$

Further, a sample of hyper-stoichiometric $UO_{2.02}$ was prepared by annealing the undoped $UO_{2.0}$ in Ar at 1473 K for 2 days. The O/U ratio was determined from a weight change before and after annealing. The result is shown in Fig. 3-2 together with the reference data of $UO_{2.0}$ [19,20]. As seen from Fig. 3-2, an anomalous increase in the heat capacity is observed above 1300 K. However, the heat capacity

value decreased above 1500 K and has almost the same value as that of $UO_{2.0}$. This reason is regarded to be a reduction of $UO_{2.02}$ to $UO_{2.0}$ above 1500 K. Since the thin oxide layer on the surface of the molybdenum thermal shield in the calorimeter has higher oxygen partial pressure than $UO_{2.02}$, molybdenum oxide layer may act as the oxygen buffer to reduce $UO_{2.02}$ to $UO_{2.00}$. As seen from Fig. 3-3, the electrical conductivity of $UO_{2.02}$ measured simultaneously with the heat capacity decreases in the temperature range from 1300 K to 1500 K, reflecting the reduction of $UO_{2.02}$.

The equation for the heat capacity of $UO_{2.02}$ below 1300 K was given by the least-squares method as :

$$C_p / \mathrm{J\ mol^{-1}\ K^{-1}} = 74.104 + 8.9822\times10^{-3}\,(T/\mathrm{K}) + 3.9178\times10^{3}\,(T/\mathrm{K})^{-1} - 2.4434\times10^{6}\,(T/\mathrm{K})^{-2},\ (296 < T/\mathrm{K} < 1300). \qquad (2)$$

3.3.2. Heat capacity of $(U_{1-y}RE_y)O_{2.0}$ (RE : trivalent rare-earth element)

Rare-earth elements are the main fission products in the nuclear fuel. Inaba et al. [3] measured the heat capacities of $(U_{1-y}Gd_y)O_2$ (y = 0.044 to 0.142) to evaluate the thermal properties under irradiation on the high-burnup oxide fuel in which high concentration gadolinium is used for the burnable poison.

In this study, several elements with different ionic radius were chosen as dopants and summarized in Table 3-2.

The heat capacities measured on $(U_{1-y}La_y)O_{2.0}$ (y = 0.044, 0.090 and 0.142), $(U_{0.91}Nd_{0.09})O_{2.0}$, $(U_{0.91}Y_{0.09})O_{2.0}$ and $(U_{0.91}Sc_{0.09})O_{2.0}$ are shown in Figs. 3-4 to 3-7. As seen from Figs. 3-4 to 3-7, an anomalous increase in the heat capacity curves similar to those of $(U_{1-y}Gd_y)O_2$ is observed. As seen from Fig. 3-4, the onset temperature for the anomalous increase of the heat capacity is the lower when the dopant

concentration is higher. Additionally from Fig. 3-8, the onset temperature (T_r) for the anomalous increase of heat capacity seems to depend on the element of dopant.

Table 3-2. The characters of dopants

Dopants	Characters
La	High fission yield, Large ionic radius
Nd	High fission yield, Stand-in for americium (Am)
Y	High fission yield, Intermediate ionic radius
Sc	Small ionic radius

The equations for the heat capacity are determined by the least-squares method from the data below onset temperature. The results are given in Table 3-3.

Table 3-3. The equations for the heat capacity of doped UO_2

Samples	a	$b\times10^{2}$	$c\times10^{-4}$	$d\times10^{-6}$	$e\times10^{-8}$	Temperature range(K)
$(U_{0.956}La_{0.044})O_{2.0}$	36.295	2.1627	4.4035	19.484	24.178	286～1200
$(U_{0.910}La_{0.090})O_{2.0}$	55.267	1.6340	2.0499	8.1166	6.2934	291～1100
$(U_{0.858}La_{0142})O_{2.0}$	43.548	2.3102	3.7635	15.823	16.582	289～1000
$(U_{0.910}Nd_{0.090})O_{2.0}$	32.001	2.3236	4.6856	21.162	28.287	298～1150
$(U_{0.910}Y_{0.090})O_{2.0}$	65.037	1.3002	0.9472	3.5600	0	295～1330
$(U_{0.910}Sc_{0.090})O_{2.0}$	57.872	1.6685	1.4078	4.6711	0	298～1300

※C_p / J mol^{-1} K^{-1} = a + b (T /K) + c (T /K)$^{-1}$-d (T /K)$^{-2}$ +e (T/K)$^{-3}$

3.3.3. Heat capacity of $(U_{1-y}Mg_y)O_{2-X}$

Magnesium and calcium are divalent cations which can form a solid solution with UO_2. Divalent cation substituted for uranium ion in the solid solution effects doubly than trivalent cations for a charge compensation. The Mg-doped UO_2 easily becomes hypo-stoichiometric composition because of its high oxygen potential [11,12,].

In this study, the heat capacity on $(U_{0.910}Mg_{0.090})O_{2.0}$, $(U_{0.850}Mg_{0.150})O_{2.0}$ and $(U_{0.850}Mg_{0.150})O_{1.92}$ were measured. As shown in Figs. 3-9 and 3-10, an anomalous increase in the heat capacity curves also appears and the onset temperature (T_r) of $(U_{0.910}Mg_{0.090})O_{2.0}$ is lower than those of $(U_{0.910}RE_{0.090})O_{2.0}$ (RE = rare earth element). As is also seen from Fig. 3-10, the onset temperature for the anomalous increase of the heat capacity of stoichiometric $UO_{2.0}$ is lower than that of hypo-stoichiometric UO_{2-X}.

The equations for the heat capacity were determined by the least-squares method from the data below the onset temperature and are given in Table 3-4.

Table 3-4. The equations for the heat capacity of Mg-doped UO_2

Samples	a	$b\times10^{3}$	$c\times10^{-3}$	$d\times10^{-6}$	$e\times10^{-7}$	Temperature range(K)
$(U_{0.910}Mg_{0.090})O_{2.0}$	66.046	11.340	8.2422	3.4889	1.3590	297～1300
$(U_{0.850}Mg_{0.150})O_{2.0}$	66.896	11.810	7.6988	3.3703	2.2650	294～800
$(U_{0.850}Mg_{0.150})O_{1.9}$	70.069	8.2599	0	1.7134	0	291～1150

※C_p / J mol^{-1} K^{-1} = a + b (T /K) + c (T /K)$^{-1}$-d (T /K)$^{-2}$ +e (T/K)$^{-3}$

3.3.4. Heat capacity of $(U_{1-y}FP_y)O_{2.0}$ (FP : simulated fission products)

A high burnup creates many fission products in the UO_2 fuel. The fission products can be classified into four groups. One is the oxides dissolved in the UO_2 matrix, second the metallic precipitates, third the oxides precipitates and last is the gases and other volatile elements [21,22]. Among these fission products, the soluble ones have the influences on the UO_2 matrix, due to defect formation and then change heat capacity. Therefore, the solid solution with the soluble fission products such as zirconium and rare-earth elements should be examined.

In this study, the simulated elements selected as the representative components of fission products are all soluble major fission products except the volatile elements and noble metals, as given in Table 3-5. Five elements (such as Zr, Ce, Pr, Nd and Y) were selected as the representative fission products and the dopant concentrations (in atomic percent) in UO_2 were determined on the basis of the table of the fission yield of stable or long-lived fission products [23], as was selected in the previous studies on

Table 3-5. The dopant concentrations simulating 2 - 10 at% burnup

Metals	Burnup / at%		
	2 at%	5 at%	10 at%
U	98.21	95.52	91.01
Zr	0.74	1.86	3.73
Ce	0.25	0.62	1.24
Pr	0.12	0.30	0.61
Nd	0.58	1.46	2.93
Y	0.10	0.24	0.49

the oxygen potential of UO_2 fuel simulating 2 - 10 atomic % (at%) burnup by Une and Oguma [13].

The results of heat capacity measurements are shown in Fig. 3-11. An anomalous increase in the heat capacity curves of each sample of $(U_{1-y}FP_y)O_2$ (y = 0.018 for 2 at% burnup, y = 0.045 for 5 at% burnup and 0.090 for 10 at% burnup) is seen above 1300, 900 and 600 K, respectively. The onset temperatures of $(U_{1-y}FP_y)O_2$ (y = 0.018, 0.045 and 0.090) are slightly low than those of $(U_{1-y}M_y)O_2$ doped with equal concentration of one kind of dopant. This fact is concluded to indicate that the existence of many kind of cations render the easy formation of oxygen defects to UO_2.

The equations for the heat capacity determined by the least-squares method from the data below onset temperature are given in Table 3-6.

Table 3-6. The equations for the heat capacity of FP-doped UO_2

Samples	a	$b \times 10^2$	$c \times 10^{-4}$	$d \times 10^{-6}$	Temperature range(K)
$(U_{0.982}FP_{0.018})O_{2.0}$	40.412	2.7569	2.1268	5.3090	298～1300
$(U_{0.955}FP_{0.045})O_{2.0}$	13.903	4.7397	3.2284	6.6604	284～850
$(U_{0.910}FP_{0.090})O_{2.0}$	17.749	5.8768	2.6822	5.8126	298～550

※C_p / J mol^{-1} K^{-1} = a + b (T /K) + c (T /K)$^{-1}$-d (T /K)$^{-2}$

3.3.5. Heat capacity of $(U_{1-y}M_y)O_{2.0}$ (M : tetra- or penta-valent element)

In the previous sections we measured the heat capacity of UO_2 doped with the cations which have a lower valence (+2 or +3) than uranium (+4) in the UO_2 matrix. Here the results on the heat capacities of UO_2 doped with the +4 or +5 valent cations are given. Titanium, zirconium, praseodymium and cerium were selected as the

tetravalent cations and niobium as the pentavalent cation. Titanium or niobium is added to UO_2 in order to improve the mechanical properties and irradiation behaviors [1], although the solubility of titanium or niobium is small. Thus, we measured the heat capacity of $(U_{0.993}Ti_{0.007})O_{2.0}$ and $(U_{0.99}Nb_{0.01})O_{2.0}$. The results are shown in Figs. 3-12 and 3-13, respectively. An anomalous increase of heat capacity was not observed for each sample, simply due to small amount of dopant concentrations.

We also measured the heat capacity of $(U_{0.910}M_{0.090})O_{2.0}$, (M = Ce, Zr and Pr). These three elements can make a solid solution with UO_2 in a wide solubility range. Cerium and praseodymium have tri- or tetra-valence in the oxides. Further, cerium is believed to act as a stand-in for neptunium of minor actinide. The results are shown in Figs. 3-14 to 3-16. An anomalous increase of heat capacity was not observed for each sample. From these observations there is no anomaly in the heat capacity in the case of UO_2 doped with tetravalent cation.

The equations for the heat capacity determined by the least-squares method from the data are shown in Table 3-7.

Table 3-7. The equations for the heat capacity of doped UO_2

Samples	a	$b \times 10^3$	$c \times 10^{-3}$	$d \times 10^{-6}$	Temperature range(K)
$(U_{0.993}Ti_{0.007})O_{2.0}$	71.089	10.405	5.3473	2.8958	298～1500
$(U_{0.990}Nb_{0.010})O_{2.0}$	75.163	8.7398	3.3420	2.5373	296～1482
$(U_{0.910}Ce_{0.090})O_{2.0}$	75.498	7.5109	0	1.5883	286～1413
$(U_{0.910}Pr_{0.090})O_{2.0}$	80.185	6.5829	0	1.8930	285～1412
$(U_{0.910}Zr_{0.090})O_{2.0}$	82.498	2.9201	0	1.9969	285～1412

※C_p / J mol^{-1} K^{-1} = a + b (T /K) + c (T /K)$^{-1}$-d (T /K)$^{-2}$

3.3.6. Enthalpies and entropies of defect formation

The excess heat capacity was evaluated by subtracting the smoothed base line of heat capacity previously determined for undoped UO_2 from the experimental heat capacity for doped UO_2. Assuming that a thermally activated process contributes to the excess heat capacity, the excess heat capacity ΔC can be expressed as : [3,5]

$$\Delta C = \frac{(\Delta H_f)^2}{\sqrt{2}RT^2} \exp\left(\frac{\Delta S_f}{2R}\right) \exp\left(\frac{-\Delta H_f}{2RT}\right), \qquad (3)$$

where ΔS_f and ΔH_f are the entropy and enthalpy of formation per Frenkel pair, respectively. The results of doped UO_2 obtained in this study are summarized in Table 3-8 and shown in Figs. 3-17 and 3-18 together with those of UO_2 [4,5,24-27] and $(U_{1-y}Gd_y)O_2$ [3] reported previously. As seen from these figures, dopant addition apparently decreases the enthalpy and the entropy of formation, and the extrapolation of the values for doped samples to zero dopant content yields the estimated values for undoped UO_2 : ΔH_f = 3.0 eV and ΔS_f = 62 J $mol^{-1}K^{-1}$, which are in good agreement with the experimental values of undoped UO_2 so far reported [4,5,25]. The value of ΔH_f for UO_2 in Fig. 3-17, thus obtained, is higher than the enthalpy of formation of an electron-hole pair, but lower than that of a Frenkel pair of oxygen, both of which were calculated theoretically by Harding et al. [24]. Although there are some ambiguities to discuss the values of ΔS_f due to large error in Fig. 3-18, the extrapolated value of ΔS_f for UO_2 seems to be higher than the entropy of formation of an electron-hole pair estimated from the electrical conductivity and the thermoelectric Seebeck coefficient of UO_2 by Hyland and Ralph [26].

It is noted that the excess heat capacity due to the formation of electron-hole pair can be expressed by :

$$\Delta C = \frac{(\Delta H_f)^2}{2RT^2}\exp\left(\frac{\Delta S_f}{2R}\right)\exp\left(\frac{-\Delta H_f}{2RT}\right), \qquad (4)$$

where $\Delta H_f'$ and $\Delta S_f'$ are the enthalpy and entropy of formation per electron-hole pair, respectively. We can see that the value of $\Delta H_f'$ equals ΔH_f in Eq. (3) and the value of $\Delta S_f'$ is 5.8 J $mol^{-1}K^{-1}$ higher than ΔS_f. Therefore, even if Eq. (4) is used instead of Eq. (3) for the analysis of excess heat capacity can give the same conclusion mentioned above.

Some typical results of the electrical conductivities of $(U,M)O_2$ measured by us in order to find the occurrence of electron-hole pair formation are shown in Fig. 3-19. The slight increase of the slope in the electrical conductivity curve is seen around 1200 K for both samples of $(U_{0.990}Nb_{0.010})O_2$ and $(U_{0.910}Sc_{0.090})O_2$ similarly to the cases of UO_2 previously measured by Matsui and Naito [28]. From the fact that (1) the temperature at which the slope changes is independent of the dopant content and is close to that of UO_2, and (2) the temperature dose not coincide with the onset temperature of the anomalous increase in the heat capacity curve especially in the case of $(U_{0.850}Mg_{0.150})O_{2.0}$, the slight increase of the slope in the conductivity curve is thought to be due to gradual transition from the extrinsic to intrinsic conduction region. It is not likely that the excess heat capacity of $(U,M)O_2$ (M = RE, Mg and FP) is due, therefore, to the formation of electron-hole pairs.

It is concluded that the anomalous increase in the heat capacity of $(U,M)O_{2-X}$ (M = RE, Mg and FP) observed at relatively low temperatures below 1300 K originates from the same mechanism as that of $(U,Gd)O_2$ and undoped UO_{2+X}, and that the predominant thermal activated process as the origin of the excess heat capacity is likely to be the formation of Frenkel pairs of oxygen.

Table 3-8. Enthalpy and entropy of formation for defects

Samples	ΔH_f (eV)	ΔS_f (J $mol^{-1}K^{-1}$)	Authors
$(U_{0.956}La_{0.044})O_{2.0}$	2.14	39.4	This study (exp.)
$(U_{0.910}La_{0.090})O_{2.0}$	1.63	34.2	This study (exp.)
$(U_{0.858}La_{0.142})O_{2.0}$	1.50	31.8	This study (exp.)
$(U_{0.910}Nd_{0.090})O_{2.0}$	2.3	48	This study (exp.)
$(U_{0.910}Y_{0.090})O_{2.0}$	1.7	34	This study (exp.)
$(U_{0.910}Sc_{0.090})O_{2.0}$	2.3	49	This study (exp.)
$(U_{0.910}Mg_{0.090})O_{2.0}$	2.5	80	This study (exp.)
$(U_{0.850}Mg_{0.150})O_{2.0}$	1.5	16	This study (exp.)
$(U_{0.850}Mg_{0.150})O_{1.9}$	2.6	83	This study (exp.)
$(U_{0.982}FP_{0.018})O_{2.0}$	2.6	53	This study (exp.)
$(U_{0.955}FP_{0.045})O_{2.0}$	1.6	34	This study (exp.)
$(U_{0.910}FP_{0.090})O_{2.0}$	1.1	23	This study (exp.)
$(U_{0.956}Gd_{0.044})O_{2.0}$	2.25	43.5	Inaba et al.[3] (exp.)
$(U_{0.927}Gd_{0.073})O_{2.0}$	1.88	40.5	Inaba et al.[3] (exp.)
$(U_{0.899}Gd_{0.101})O_{2.0}$	1.45	26.9	Inaba et al.[3] (exp.)
$(U_{0.858}Gd_{0.142})O_{2.0}$	1.10	25.1	Inaba et al.[3] (exp.)
UO_2	1.86	6.11	Hyland and Ralph [26] (cal. for e-h pairs)
UO_2	5.12-5.20	-4.18	Harding et al.[24] (cal. for Frenkel defects)
UO_2	1.64-1.74	28.5-30.5	Harding et al.[24] (cal. for e-h pairs)
UO_2	3.11	62.0	Szwarc [5] (exp.)

※ exp. : experimental value from the excess heat capacity.
cal. : theoretical calculation.

By doping trivalent cations such as La^{3+}, Nd^{3+}, Y^{3+}, Sc^{3+} and Gd^{3+} or divalent Mg^{2+} into UO_2, U^{5+} ions with smaller ionic radius than that of U^{4+} ions are formed from the electroneutrality condition, and then the Frenkel pairs of oxygen could be easily formed at low temperature.

3.3.7. A relation between lattice distortion and onset temperature for a rapid increase of heat capacity

In the preceding section a close relation among the anomalous increase in heat capacity, the species and concentration of dopant was discussed.

In this section we consider the relation between the onset temperatures for the heat capacity anomaly and lattice distortion (lattice constant).

At first we examine the relation of onset temperature with a change of lattice constant. In Fig. 3-20 the onset temperatures (T_r) of UO_2 doped with various cations are plotted against $|\Delta a|$, where $|\Delta a|$ is the absolute value of the change in the lattice constant of UO_2 due to formation of a substitutional solid solution with aliovalent cations. The change in the lattice constant Δa was calculated by the following empirical equation (5) previously proposed by Kim [30]:

$$\begin{aligned} a &= 0.5648 + [0.0206(r_d - r_u) + 0.00013(Z_d - Z_u)]m \\ &= 0.5648 + \Delta am, \end{aligned} \qquad (5)$$

where a and 0.5648 (in nanometers) is the lattice constant of doped UO_2 and that of undoped UO_2, respectively, (r_d - r_u) is the difference between ionic radii of doped element (r_d) and host uranium (r_u), (Z_d - Z_u) is the valency difference, and m is the mole percent of the dopant in the form of MO_X. In this calculation the values of ionic radii were taken from Shannon's table [31]. The validity of this kind of

empirical equations for the change of the lattice constant has been demonstrated by the remarkable agreement between the calculated and measured values of the lattice constants for the fluorite-type oxide doped with various cations such as Ca, Mg, Sr, Sc, Y, Sm, Gd and Eu [30]. It is seen from Fig. 3-20 that the onset temperature of the doped UO_2 with same dopant concentration increases with increasing $|\Delta a|$, indicating the smaller elastic strain field produces the lower onset temperature of the heat capacity anomaly since the elastic energy in the strained lattice is linearly proportional to $(m \Delta a)^2$ in a fluorite-type oxide [32]. As seen from Figs. 3-17 and 3-18 the enthalpy and entropy of formation calculated from the excess heat capacity of $(U_{0.910}Sc_{0.090})O_{2.0}$ are also a little higher than those of $(U_{0.910}La_{0.090})O_{2.0}$. Therefore the formation of Frenkel defect of oxygen is considered to be suppressed by the elastic strain. The fact that the ionic conductivity of doped fluorite-type oxides (such as $(Ce,M)O_2$, M = Gd, Y and La), where the oxygen ion is predominantly mobile, decreases with increasing $|\Delta a|$ as reviewed by Kim [30] also supports the validity of the dependence of the onset temperatures upon $|\Delta a|$ values, since the Frenkel defect of oxygen can be formed more easily under the condition which makes oxygen ions more mobile. For UO_2 doped with the same cation, the onset temperature is seen to decrease with increasing dopant concentration as shown in Fig. 3-20. The lower onset temperatures of $(U_{1-y}Gd_y)O_2$ and $(U_{1-y}La_y)O_{2.0}$ with higher dopant concentrations are related to the lower enthalpy and entropy of formation shown in Figs. 3-17 and 3-18. In other words, the formation of a large number of Frenkel defects composed of oxygen vacancies produced by doping the large amount of trivalent cations and the compensating oxygen interstitials caused from the stoichiometric condition (O/M = 2.00) may decrease the onset temperature, since the heat capacity anomaly appears

when the defect concentration becomes significantly large [6].

In Fig. 3-20 the onset temperatures of $(U,FP)O_{2.0}$, however, are seen to be apart from the straight lines which represent the onset temperatures of UO_2 doped with a single cation, $(U,M)O_{2.0}$.

The local structural environments of Y^{3+} and Zr^{4+} ions in 18 weight % (wt%) Y_2O_3 doped ZrO_2 were studied using extended X-ray absorption fine structure (EXAFS) spectroscopy over the temperature range 153 - 1043 K [33]. The oxygen arrangements around Y^{3+} and Zr^{4+} were found to be different from each other, i.e. more oxygen vacancies were sited adjacent to Zr^{4+} and were more disordered than Y^{3+} at low temperature. The temperature rise of the sample makes the local structural environments of two different cations more alike, suggesting that increase in the oxygen mobility enhances random in the spatial distribution of oxygen defects. Therefore, similarly to the case of ZrO_2, the oxygen arrangement around M^{3+} dopants in UO_2, which has the same fluorite structure as ZrO_2, is regarded to be different from that around uranium ions. It is also expected that oxygen defects around M^{3+} and U^{4+} become more dispersive (disorder) with increasing temperature, resulting in the heat capacity anomaly.

Next, the variety of the oxygen arrangement around cations in UO_2 is assumed to relate to the value of ΔX expressed by Eq. (6), i.e. the difference between the average cation-oxygen interatomic distances calculated from the ionic radii in Shannon's table [31] and obtained from the experimental lattice constants of doped UO_2 based on the perfect fluorite structure :

$$\Delta X = \left[(r_c + r_o) - \frac{\sqrt{3}}{4}a_1\right]_A - \left[(r_u + r_o) - \frac{\sqrt{3}}{4}a_2\right]_B , \qquad (6)$$

where A and B represent the doped UO_2 and undoped UO_2, respectively. The values of r_c, r_o and r_u which are the average ionic radius of all cations (M^{3+}, U^{4+}, U^{5+}) with eightfold coordination in doped UO_2, the ionic radius of an oxygen ion with fourfold coordination and the ionic radius of a uranium ion with eightfold coordination, respectively, were taken from the paper by Shannon [31]. The values of the lattice constants of doped UO_2 (a_1) and undoped UO_2 (a_2) were given experimentally [13,30,33-37]. As can be seen from Fig. 3-21, the onset temperatures (T_r) of the heat capacity anomaly of $(U_{1-y}M_y)O_{2-X}$ (where M is Gd, La, Nd, Eu, Sc, Mg and FP; y = 0.018 - 0.142) were found to decrease linearly with increasing $|\Delta X|$. This indicates that the larger is the change in the average cation-oxygen interatomic distance (i.e. the more complicated distribution of oxygen defects) caused by the introduction of an aliovalent cation, the lower becomes the onset temperature. Further, the values for all the doped UO_2 with the exception of Mg, Sc and FP, fall on the same straight line irrespective of the dopant and its concentration. In the case of UO_2 doped with Mg and Sc, their onset temperatures plotted as a function of $|\Delta X|$ fall on a different straight line, as shown in Fig. 3-21. This different dependence of the onset temperatures on ΔX may be due to the formation of cation defect clusters composed of Mg^{2+} (or Sc^{3+}) and U^{5+}, since (1) the ionic radii of Mg^{2+} and Sc^{3+} are smaller than that of U^{4+}, different from other trivalent cations, i.e. $\Delta X < 0$ for Mg^{2+} and Sc^{3+} and $\Delta X > 0$ for other cations, and (2) the presence of the formation of cation defect clusters (Mg^{2+} - U^{5+}) has been previously proposed on the bases of the data of the oxygen potential of $(U_{1-y}Mg_y)O_2$ [40]. Slightly higher values of the enthalpies of formation for a Frenkel-pair of oxygen in $(U_{1-y}M_y)O_2$ (M = Mg and Sc), in Fig. 3-17, are assumed to originate from the formation of such metal clusters.

The onset temperatures of $(U_{1-y}FP_y)O_{2.0}$ are also seen to deviate from the line with increasing ΔX (i.e. y value). Because the value of ΔX for $(U_{1-y}FP_y)O_{2.0}$ was calculated from the average cation radii of many kinds of cations (Nd^{3+}, Y^{3+}, Ce^{4+}, Pr^{4+}, Zr^{4+}, U^{4+}, U^{5+}) using Eq. (6) by the same procedure as for UO_2 doped with a single cation, the variety (complexity) of the local structures of oxygens (or degree of disordering of the oxygen arrangement) around cations is not considered to be suitably expressed by the ΔX value alone.

It is also noted in Fig. 3-21 that the onset temperatures of UO_2 doped with Pr^{4+}, Ce^{4+} and Zr^{4+} are obtained on the assumption of the presence of the heat capacity anomaly and of the same linear relation between $|\Delta X|$ and T_r. The determined onset temperatures of UO_2 doped with tetravalent praseodymium, cerium and zirconium ions, thus estimated, are higher than 1420 K which is above the upper temperature limit of the heat capacity measurements in the present study. It is, therefore, not clear at present whether the heat capacity anomaly in UO_2 doped with these tetravalent cations exists. To make clear the validity of the above assumption, more precise structural analysis by EXAFS was performed and the result is given in the next chapter.

3.3.8. Thermal functions

The enthalpy increment, entropy and free energy function (*fef*) of $(U_{1-y}M_y)O_{2-x}$ were calculated from the heat capacity and the entropy S^o_{298} using the following fundamental thermodynamic equations, respectively:

$$H^o_T - H^o_{298} = \int_{298}^{T} C_p \, dT \tag{7}$$

$$S^o_T = S^o_{298} + \int_{298}^{T} (C_p / T) dT \tag{8}$$

$$-(G_T^o - H_{298}^o)/T = -(fef) = -(H_T^o - H_{298}^o)/T + S_T^o. \quad (9)$$

The S^o_{298} value required for the above computations was estimated from the literature data [40] of S^o_{298} values for UO_2 and MO_X by using the additivity law as a first approximation. The results of the thermal functions are given in Tables 3-9 to 3-27.

Table 3-9 Thermal functions of $UO_{2.0}$

Temperature (K)	C_p (J mol^{-1} K^{-1})	$S°_T$ (J mol^{-1} K^{-1})	$H°_T$-$H°_{298.15}$ (kJ mol^{-1})	-($G°_T$-$H°_{298.15}$)/T (J mol^{-1} K^{-1})
298.15	60.24	77.03	0.00	77.03
300	60.58	77.40	0.11	77.40
400	71.81	96.62	6.82	96.61
500	76.68	113.23	14.27	113.20
600	79.35	127.47	22.08	127.43
700	81.13	139.84	30.11	139.80
800	82.51	150.77	38.30	150.72
900	83.69	160.55	46.61	160.50
1000	84.79	169.43	55.03	169.37
1100	85.85	177.56	63.56	177.50
1200	86.89	185.08	72.20	185.02
1300	87.93	192.07	80.94	192.01
1400	88.97	198.63	89.79	198.56
1500	90.02	204.80	98.74	204.73

Table 3-10 Thermal functions of $UO_{2.02}$

Temperature (K)	C_p (J mol^{-1} K^{-1})	$S°_T$ (J mol^{-1} K^{-1})	$H°_T$-$H°_{298.15}$ (kJ mol^{-1})	-($G°_T$-$H°_{298.15}$)/T (J mol^{-1} K^{-1})
298.15	62.44	79.08	0.00	79.08
300	62.71	79.47	0.12	79.47
400	72.22	99.01	6.93	98.99
500	76.66	115.66	14.40	115.63
600	79.24	129.88	22.20	129.84
700	81.00	142.23	30.22	142.19
800	82.37	153.14	38.39	153.09
900	83.52	162.91	46.69	162.86
1000	84.56	171.76	55.09	171.71
1100	85.53	179.87	63.60	179.81
1200	86.45	187.35	72.20	187.29
1300	87.35	194.31	80.89	194.24

Table 3-11 Thermal functions of $(U_{0.956}La_{0.044})O_{2.0}$

Temperature (K)	C_p (J mol^{-1} K^{-1})	$S°_T$ (J mol^{-1} K^{-1})	$H°_T$-$H°_{298.15}$ (kJ mol^{-1})	-($G°_T$-$H°_{298.15}$)/T (J mol^{-1} K^{-1})
298.15	62.48	77.20	0.00	77.20
300	62.63	77.58	0.12	77.58
400	71.04	96.78	6.81	96.77
500	76.58	113.29	14.22	113.26
600	79.73	127.56	22.05	127.52
700	81.63	140.00	30.12	139.96
800	82.92	150.99	38.35	150.94
900	83.95	160.82	46.70	160.77
1000	84.89	169.71	55.14	169.66
1100	85.83	177.85	63.68	177.79
1200	86.81	185.36	72.31	185.30

Table 3-12 Thermal functions of $(U_{0.910}La_{0.090})O_{2.0}$

Temperature (K)	C_p (J mol^{-1} K^{-1})	$S°_T$ (J mol^{-1} K^{-1})	$H°_T$-$H°_{298.15}$ (kJ mol^{-1})	-($G°_T$-$H°_{298.15}$)/T (J mol^{-1} K^{-1})
298.15	61.33	77.93	0.00	77.93
300	61.62	78.31	0.11	78.31
400	72.16	97.69	6.88	97.67
500	77.00	114.37	14.36	114.34
600	79.60	128.66	22.20	128.62
700	81.26	141.06	30.25	141.02
800	82.51	152.00	38.44	151.95
900	83.59	161.78	46.75	161.73
1000	84.62	170.64	55.16	170.59
1100	85.64	178.75	63.67	178.70

Table 3-13 Thermal functions of $(U_{0.858}La_{0.142})O_{2.0}$

Temperature (K)	C_p (J mol^{-1} K^{-1})	$S°_T$ (J mol^{-1} K^{-1})	$H°_T$-$H°_{298.15}$ (kJ mol^{-1})	-($G°_T$-$H°_{298.15}$)/T (J mol^{-1} K^{-1})
298.15	61.23	79.02	0.00	79.02
300	61.53	79.40	0.11	79.40
400	73.89	98.97	6.95	98.96
500	80.34	116.23	14.69	116.20
600	83.86	131.22	22.92	131.18
700	86.03	144.32	31.42	144.28
800	87.59	155.92	40.11	155.86
900	88.90	166.31	48.93	166.25
1000	90.12	175.74	57.88	175.68

Table 3-14 Thermal functions of $(U_{0.910}Nd_{0.090})O_{2.0}$

Temperature (K)	C_p (J mol^{-1} K^{-1})	$S°_T$ (J mol^{-1} K^{-1})	$H°_T$-$H°_{298.15}$ (kJ mol^{-1})	-($G°_T$-$H°_{298.15}$)/T (J mol^{-1} K^{-1})
298.15	64.75	79.33	0.00	79.33
300	64.79	79.73	0.12	79.73
400	70.37	99.06	6.85	99.05
500	75.31	115.34	14.16	115.31
600	78.35	129.36	21.85	129.32
700	80.26	141.59	29.79	141.55
800	81.62	152.40	37.89	152.36
900	82.73	162.08	46.10	162.03
1000	83.76	170.85	54.43	170.80
1100	84.79	178.88	62.86	178.83

Table 3-15 Thermal functions of $(U_{0.910}Y_{0.090})O_{2.0}$

Temperature (K)	C_p (J mol^{-1} K^{-1})	$S°_T$ (J mol^{-1} K^{-1})	$H°_T$-$H°_{298.15}$ (kJ mol^{-1})	-($G°_T$-$H°_{298.15}$)/T (J mol^{-1} K^{-1})
298.15	60.63	76.66	0.00	76.66
300	60.96	77.03	0.11	77.03
400	71.67	96.28	6.83	96.27
500	76.24	112.83	14.25	112.80
600	78.74	126.97	22.01	126.93
700	80.40	139.24	29.97	139.19
800	81.72	150.06	38.08	150.01
900	82.87	159.75	46.31	159.70
1000	83.95	168.54	54.65	168.49
1100	85.01	176.59	63.10	176.53
1200	86.06	184.03	71.65	183.97
1300	87.12	190.96	80.31	190.90

Table 3-16 Thermal functions of $(U_{0.910}Sc_{0.090})O_{2.0}$

Temperature (K)	C_p (J mol^{-1} K^{-1})	$S°_T$ (J mol^{-1} K^{-1})	$H°_T$-$H°_{298.15}$ (kJ mol^{-1})	-($G°_T$-$H°_{298.15}$)/T (J mol^{-1} K^{-1})
298.15	57.52	75.66	0.00	75.66
300	57.90	76.02	0.11	76.02
400	70.55	94.71	6.64	94.70
500	75.69	111.08	13.98	111.05
600	78.37	125.14	21.69	125.10
700	80.13	137.36	29.62	137.32
800	81.52	148.15	37.71	148.10
900	82.76	157.83	45.92	157.78
1000	83.96	166.61	54.26	166.55
1100	85.16	174.67	62.72	174.61
1200	86.38	182.13	71.29	182.07
1300	87.63	189.09	79.99	189.03

Table 3-17 Thermal functions of $(U_{0.910}Mg_{0.090})O_{2.0}$

Temperature (K)	C_p (J mol^{-1} K^{-1})	$S°_T$ (J mol^{-1} K^{-1})	$H°_T$-$H°_{298.15}$ (kJ mol^{-1})	-($G°_T$-$H°_{298.15}$)/T (J mol^{-1} K^{-1})
298.15	58.34	79.24	0.00	79.24
300	58.66	79.60	0.11	79.60
400	69.59	98.22	6.61	98.20
500	74.35	114.32	13.83	114.29
600	76.96	128.13	21.41	128.09
700	78.68	140.13	29.19	140.08
800	80.00	150.72	37.13	150.67
900	81.12	160.21	45.19	160.16
1000	82.15	168.81	53.35	168.76
1100	83.14	176.69	61.62	176.63
1200	84.11	183.96	69.98	183.90
1300	85.07	190.73	78.44	190.67

Table 3-18 Thermal functions of $(U_{0.850}Mg_{0.150})O_{2.0}$

Temperature (K)	C_p (J mol^{-1} K^{-1})	$S°_T$ (J mol^{-1} K^{-1})	$H°_T$-$H°_{298.15}$ (kJ mol^{-1})	-($G°_T$-$H°_{298.15}$)/T (J mol^{-1} K^{-1})
298.15	59.18	81.38	0.00	81.38
300	59.49	81.75	0.11	81.75
400	70.16	100.56	6.67	100.55
500	74.90	116.79	13.95	116.76
600	77.56	130.70	21.59	130.66
700	79.35	142.79	29.44	142.75
800	80.75	153.48	37.44	153.44

Table 3-19 Thermal functions of $(U_{0.850}Mg_{0.150})O_{1.9}$

Temperature (K)	C_p (J mol^{-1} K^{-1})	$S°_T$ (J mol^{-1} K^{-1})	$H°_T$-$H°_{298.15}$ (kJ mol^{-1})	-($G°_T$-$H°_{298.15}$)/T (J mol^{-1} K^{-1})
298.15	53.26	71.13	0.00	71.13
300	53.51	71.46	0.10	71.46
400	62.66	88.28	5.97	88.26
500	67.35	102.81	12.49	102.79
600	70.27	115.37	19.38	115.33
700	72.35	126.36	26.51	126.32
800	74.00	136.13	33.84	136.09
900	75.39	144.93	41.31	144.89
1000	76.62	152.94	48.91	152.89
1100	77.74	160.29	56.63	160.24

Table 3-20 Thermal functions of $(U_{0.982}FP_{0.018})O_{2.0}$

Temperature (K)	C_p (J mol^{-1} K^{-1})	$S°_T$ (J mol^{-1} K^{-1})	$H°_T$-$H°_{298.15}$ (kJ mol^{-1})	-($G°_T$-$H°_{298.15}$)/T (J mol^{-1} K^{-1})
298.15	60.24	76.15	0.00	76.15
300	60.59	76.52	0.11	76.52
400	71.43	95.73	6.81	95.71
500	75.50	112.16	14.19	112.13
600	77.65	126.13	21.85	126.10
700	79.26	138.23	29.70	138.18
800	80.76	148.91	37.70	148.86
900	82.30	158.51	45.85	158.46
1000	83.94	167.26	54.16	167.21
1100	85.68	175.34	62.64	175.29
1200	87.53	182.88	71.30	182.82
1300	89.47	189.96	80.15	189.90

Table 3-21 Thermal functions of $(U_{0.955}FP_{0.045})O_{2.0}$

Temperature (K)	C_p (J mol^{-1} K^{-1})	$S°_T$ (J mol^{-1} K^{-1})	$H°_T$-$H°_{298.15}$ (kJ mol^{-1})	-($G°_T$-$H°_{298.15}$)/T (J mol^{-1} K^{-1})
298.15	61.39	75.44	0.00	75.44
300	61.73	75.82	0.11	75.82
400	71.94	95.27	6.90	95.26
500	75.53	111.76	14.30	111.74
600	77.65	125.73	21.96	125.69
700	79.61	137.84	29.82	137.80
800	81.77	148.61	37.89	148.57

Table 3-22 Thermal functions of $(U_{0.910}FP_{0.090})O_{2.0}$

Temperature (K)	C_p (J mol^{-1} K^{-1})	$S°_T$ (J mol^{-1} K^{-1})	$H°_T$-$H°_{298.15}$ (kJ mol^{-1})	-($G°_T$-$H°_{298.15}$)/T (J mol^{-1} K^{-1})
298.15	59.84	78.43	0.00	78.43
300	60.20	78.80	0.11	78.80
400	71.98	98.01	6.82	97.99
500	77.53	114.72	14.31	114.69

Table 3-23 Thermal functions of $(U_{0.993}Ti_{0.007})O_{2.0}$

Temperature (K)	C_p (J mol^{-1} K^{-1})	$S°_T$ (J mol^{-1} K^{-1})	$H°_T$-$H°_{298.15}$ (kJ mol^{-1})	-($G°_T$-$H°_{298.15}$)/T (J mol^{-1} K^{-1})
298.15	59.55	76.50	0.00	76.50
300	59.86	76.87	0.11	76.86
400	70.52	95.77	6.71	95.76
500	75.40	112.09	14.03	112.07
600	78.20	126.11	21.72	126.07
700	80.10	138.31	29.64	138.27
800	81.57	149.11	37.73	149.06
900	82.82	158.79	45.95	158.74
1000	83.95	167.58	54.29	167.52
1100	85.00	175.63	62.74	175.57
1200	86.02	183.07	71.29	183.01
1300	87.02	189.99	79.94	189.93
1400	88.00	196.48	88.69	196.41
1500	88.97	202.58	97.54	202.51

Table 3-24 Thermal functions of $(U_{0.990}Nb_{0.001})O_{2.0}$

Temperature (K)	C_p (J mol^{-1} K^{-1})	$S°_T$ (J mol^{-1} K^{-1})	$H°_T$-$H°_{298.15}$ (kJ mol^{-1})	-($G°_T$-$H°_{298.15}$)/T (J mol^{-1} K^{-1})
298.15	60.43	76.34	0.00	76.34
300	60.73	76.71	0.11	76.71
400	71.16	95.83	6.78	95.81
500	76.07	112.29	14.17	112.26
600	78.93	126.43	21.93	126.40
700	80.88	138.75	29.92	138.71
800	82.37	149.65	38.09	149.61
900	83.61	159.43	46.39	159.38
1000	84.71	168.30	54.81	168.24
1100	85.72	176.42	63.33	176.36
1200	86.67	183.92	71.95	183.86
1300	87.59	190.89	80.66	190.83
1400	88.49	197.42	89.47	197.35

Table 3-25 Thermal functions of $(U_{0.910}Ce_{0.090})O_{2.0}$

Temperature (K)	C_p (J mol^{-1} K^{-1})	$S°_T$ (J mol^{-1} K^{-1})	$H°_T$-$H°_{298.15}$ (kJ mol^{-1})	-($G°_T$-$H°_{298.15}$)/T (J mol^{-1} K^{-1})
298.15	59.87	73.19	0.00	73.19
300	60.10	73.56	0.11	73.56
400	68.58	92.17	6.60	92.15
500	72.90	107.98	13.69	107.95
600	75.59	121.53	21.13	121.49
700	77.51	133.33	28.79	133.29
800	79.03	143.78	36.62	143.74
900	80.30	153.17	44.58	153.12
1000	81.42	161.68	52.67	161.63
1100	82.45	169.49	60.87	169.44
1200	83.41	176.71	69.16	176.65
1300	84.32	183.42	77.55	183.36
1400	85.20	189.70	86.02	189.64

Table 3-26 Thermal functions of $(U_{0.910}Pr_{0.090})O_{2.0}$

Temperature (K)	C_p (J mol^{-1} K^{-1})	$S°_T$ (J mol^{-1} K^{-1})	$H°_T$-$H°_{298.15}$ (kJ mol^{-1})	-($G°_T$-$H°_{298.15}$)/T (J mol^{-1} K^{-1})
298.15	60.85	74.77	0.00	74.77
300	61.13	75.15	0.11	75.15
400	70.99	94.28	6.78	94.26
500	75.90	110.70	14.15	110.67
600	78.88	124.82	21.90	124.78
700	80.93	137.14	29.90	137.10
800	82.49	148.05	38.07	148.01
900	83.77	157.85	46.39	157.79
1000	84.87	166.73	54.82	166.67
1100	85.86	174.87	63.36	174.81
1200	86.77	182.38	71.99	182.32
1300	87.62	189.36	80.71	189.29
1400	88.44	195.88	89.51	195.82

Table 3-27 Thermal functions of $(U_{0.910}Zr_{0.090})O_{2.0}$

Temperature (K)	C_p (J mol^{-1} K^{-1})	$S°_T$ (J mol^{-1} K^{-1})	$H°_T$-$H°_{298.15}$ (kJ mol^{-1})	-($G°_T$-$H°_{298.15}$)/T (J mol^{-1} K^{-1})
298.15	60.90	72.11	0.00	72.11
300	61.19	72.49	0.11	72.49
400	71.19	91.66	6.80	91.65
500	75.97	108.12	14.18	108.09
600	78.70	122.23	21.93	122.19
700	80.47	134.50	29.89	134.46
800	81.71	145.33	38.00	145.29
900	82.66	155.02	46.23	154.96
1000	83.42	163.77	54.53	163.71
1100	84.06	171.75	62.91	171.69
1200	84.62	179.09	71.34	179.03
1300	85.11	185.88	79.83	185.82
1400	85.57	192.20	88.36	198.06

3.4. Conclusions

The following conclusions were drawn in the chapter 3.

(1) An anomalous increase in the heat capacity curves of $(U_{1-y}RE_y)O_{2.0}$ (where RE is La, Nd, Y and Sc), $(U_{1-y}Mg_y)O_{2-X}$ (x = 0 and 0.1) and $(U_{1-y}FP_y)O_{2.0}$ (where FP is simulated fission products, Zr, Nd, Ce, Y and Pr) was observed over the temperature range from 600 to 1300 K.

(2) The heat capacity anomaly originate from the same mechanism as that of undoped UO_2, and the predominantly thermal activated process to produce the excess heat capacity is likely to be the formation of the Frenkel pair-like defect of oxygen.

(3) No anomalous increase in the heat capacity curves of $(U_{1-y}M_y)O_{2.0}$ (where M is Pr, Ce, Zr, Ti and Nb) was observed over the temperature range up to 1410 K for Zr, Ce and Pr and up to 1500 K for Ti and Nb in contrast to the cases of $(U_{1-y}RE_y)O_{2.0}$ (where RE is La, Nd, Y, Sc, Mg and simulated fission products).

(4) The occurrence of the heat capacity anomaly of doped UO_2 originate predominately in oxygen defects formed from the electroneutrality condition by the introduction of aliovalent (trivalent or divalent) cations in UO_2. Therefore, the introduction of the tetravalent cations (Pr, Ce, Zr and Ti) results in an insignificant effect on the production of oxygen defects, producing no heat capacity anomaly.

(5) The onset temperatures of the heat capacity anomaly observed for doped UO_2 increase with increasing the lattice parameter change. It suggests that the large elastic strain suppresses the formation of the Frenkel pair-like defect of oxygen, thus, it increases the onset temperature.

References

[1] J.C.Killeen, *J. Nucl. Mater.*, **58** (1975) 39.

[2] H.Inaba, K.Naito, M.Oguma and H.Masuda, *J. Nucl. Mater.*, **137** (1986) 176.

[3] H.Inaba, Knaito and M.Oguma, *J. Nucl. Mater.*, **149** (1987) 342.

[4] J.F.Kerrisk and D.G.Clifton, *Nucl. Technol.*, **16** (1972) 531.

[5] R.Szwarc, *J. Phys. Chem. Solids*, **30** (1969) 705.

[6] K.Naito, *J. Nucl. Mater.*, **167** (1989) 30.

[7] T.Matsui and K.Naito, *J. Nucl. Mater.*, **138** (1986) 19.

[8] K.Une and M.Oguma, *J. Nucl. Mater.*, **118** (1983) 189.

[9] K.Hagemark and M.Broli, *J. Am. Ceram. Soc.*, **50** (1967) 563.

[10] Y.Hinatsu and T.Fujino, *J. Solid State Chem.*, **62** (1986) 342.

[11] T.Fujino and K.Naito, *J. inorg. nucl. chem.*, **32** (1970) 627.

[12] T.Fujino, J.Tateno and H.Tagawa, *J. Solid State Chem.*, **24** (1978) 11.

[13] K.Une and M.Oguma, *J. Nucl. Sci. Technol.*, **20** (1983) 844.

[14] T.Tsuji, T.Matsui, M.Abe and K.Naito, *J. Nucl. Mater.*, **168** (1989) 151.

[15] T.L.Markin and E.C.Crough, *J. inorg. nucl. chem.*, **32** (1970) 77.

[16] T.Yamashita and T.Fujino, Paper presented at the *Annual Meeting of the Japan Atomic Energy Society*, Tokyo, Japan (1989) J3.

[17] S.Aronson and J.C.Clayton, *J. Chem. Phys.*, **35** (1961) 1055.

[18] T.Matsui and K.Naito, *J. Nucl. Mater.*, **136** (1985) 59.

[19] F.Grönvold, N.J.Kveseth, A.Sveen and J.Tichy, *J. Chem. Thermodyn.*, **2** (1970) 665.

[20] D.R.Fredrickson and M.G.Chasanov, *J. Chem. Thermodyn.*, **2** (1970) 623.

[21] H.Kleycamp, *J. Nucl. Mater.*, **131** (1985) 221.

[22] S.Imoto, *J. Nucl. Mater.*, **140** (1986) 19.

[23] M.E.Meek and B.F.Rider, *Technical Report NEDO*-12154, General Electric Company, CA, 1972.

[24] J.H.Harding, P.Masri and A.M.Stoneham, *J. Nucl. Mater.*, **92** (1980) 73.

[25] P.Browning, *J. Nucl. Mater.*, **98** (1981) 345.

[26] G.Hyland and J.Ralph, *High Temp.- High Press.*, **15** (1983) 179.

[27] K.Clausen, W.Hayes, J.E.Macdonald and R.Osborn, *Phys. Rev. Lett.*, **52** (1984) 1238.

[28] T.Matsui and K.Naito, *J. Nucl. Mater.*, **138** (1986) 19.

[29] R.A.Jackson, C.Richard, A.Catlow and D.Murray, *J. Chem. Soc. Faraday Trsans.*2, **83** (1987) 1171.

[30] D.J.Kim, *J. Am. Ceram. Soc.*, **72** (1979) 1415.

[31] D.Shannon, *Acta Cryst.*, **A32** (1976) 751.

[32] L.S.Darken and R.W.Gurry, in : *Physical Chemistry of Metals* (McGraw-Hill, New York, 1953) p.74.

[33] C.R.A.Catlow, A.V.Chadwick, G.N.Greaves and L.M.Moroney, *J. Am. Ceram. Soc.*, **69** (1986) 272.

[34] W.A.Young, L.Lynds and J.S.Mohl, NAA-SR-6765, USA, 1962.

[35] T.Ohmichi, S.Fukushima, M.Maeda and H.Watanabe, *J. Nucl. Mater.*, **102** (1981) 40.

[36] T.Yamashita, T.Fujino and H.Tagawa, *J. Nucl. Mater.*, **132** (1985) 192.

[37] D.I.R.Norris and P.Kay, *J. Nucl. Mater.*, **116** (1983) 184.

[38] S.Aronson and J.C.Clayton, *J. Chem. Phys.*, **35** (1961) 1055.

[39] T.Matsui, T.Kawase and K.Naito, *J. Nucl. Mater.*, **186** (1992) 254.

[40] T.Fujino and N.Sata, *J. Nucl. Mater.*, **189** (1992) 103.

[41] I.Barin, *"Thermochemical Data of Pure Substances."*, VCH, Weinheim, Germany, 1989

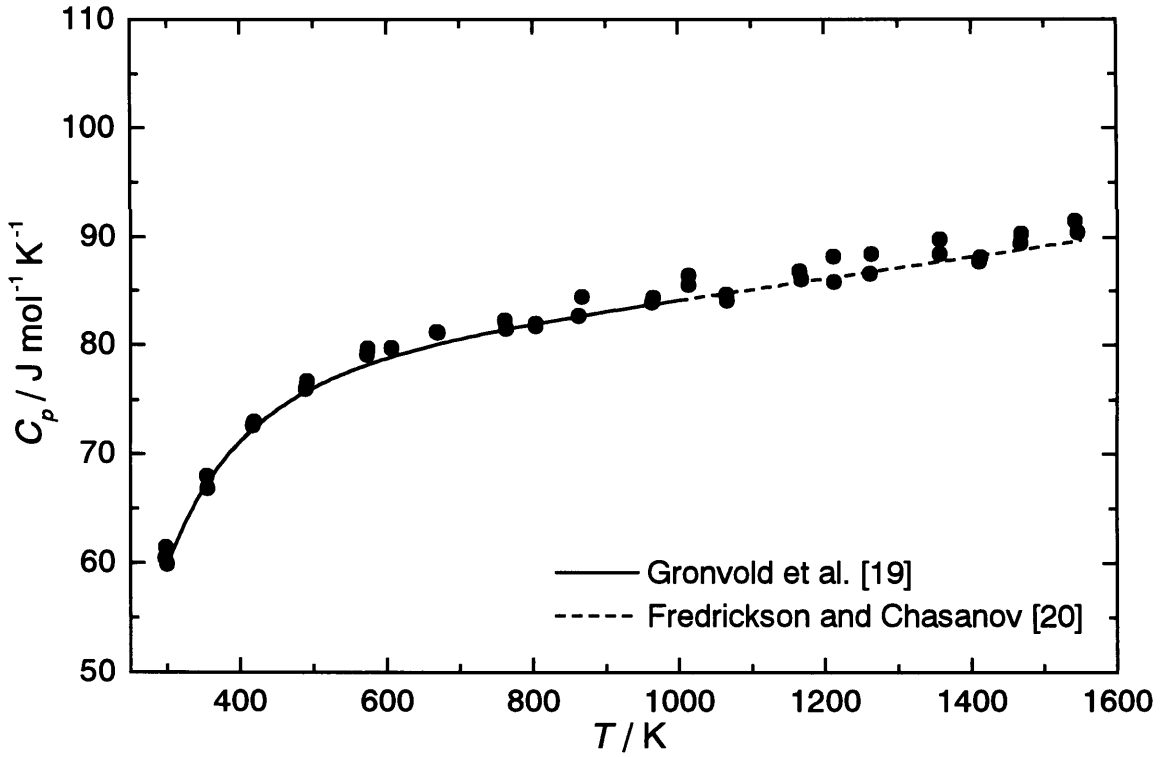

Fig.3-1 Heat capacity of $UO_{2.0}$.

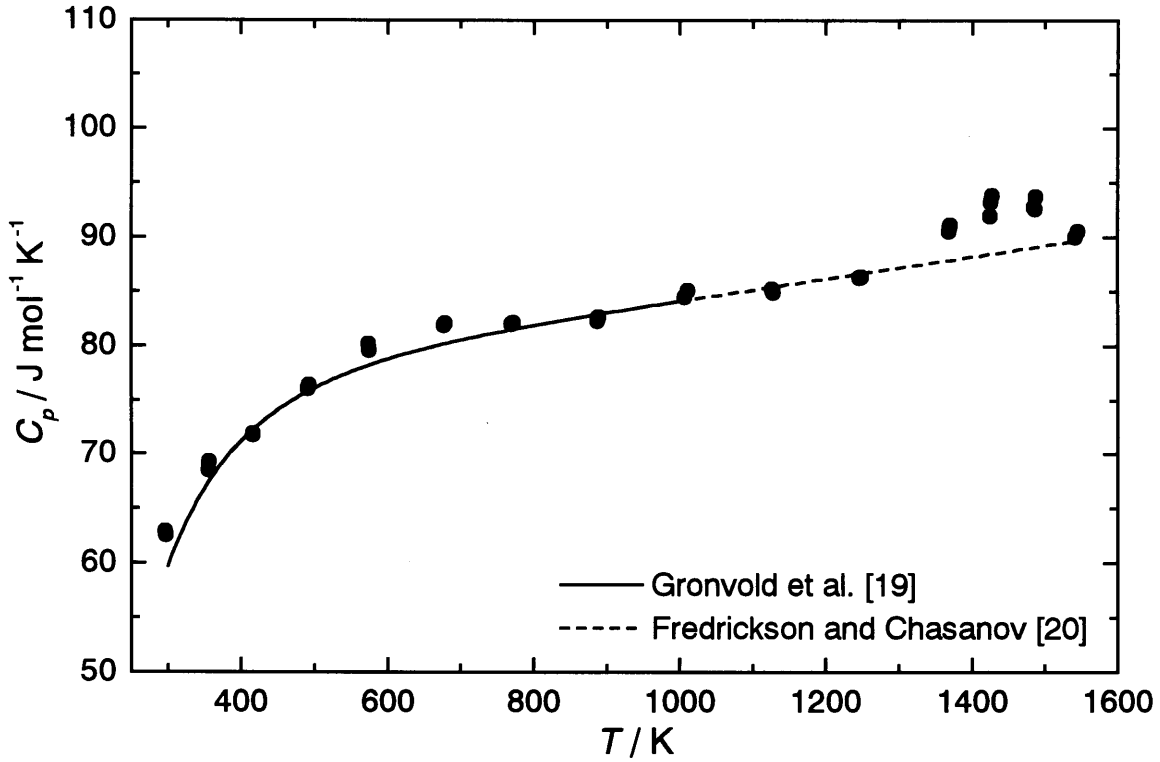

Fig.3-2 Heat capacity of $UO_{2.02}$.

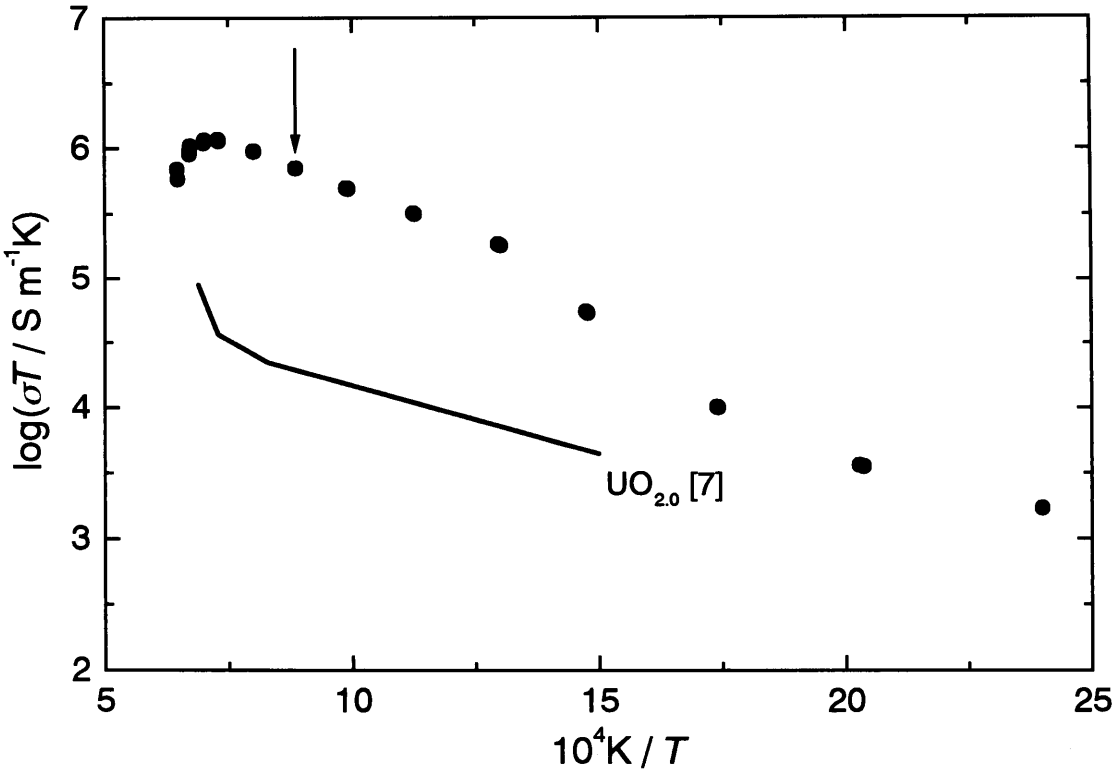

Fig.3-3 Electrical conductivity of $UO_{2.02}$.

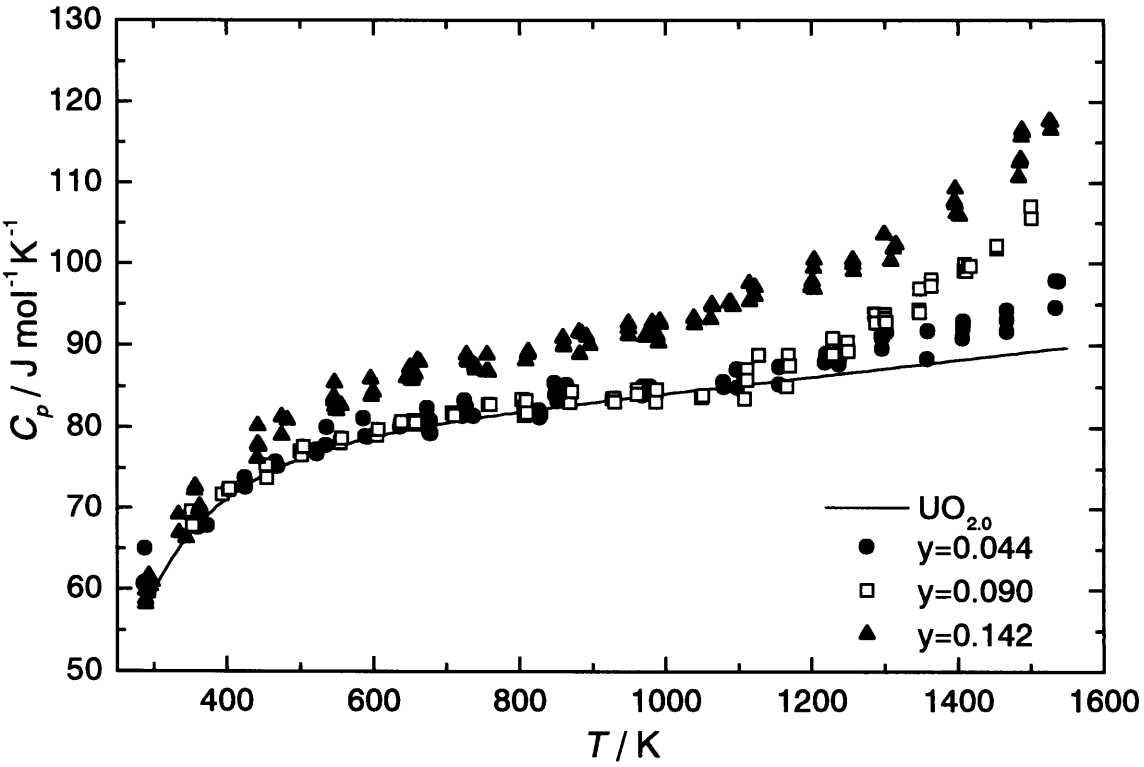

Fig.3-4 Heat capacity of $(U_{1-y}La_y)O_{2.0}$.

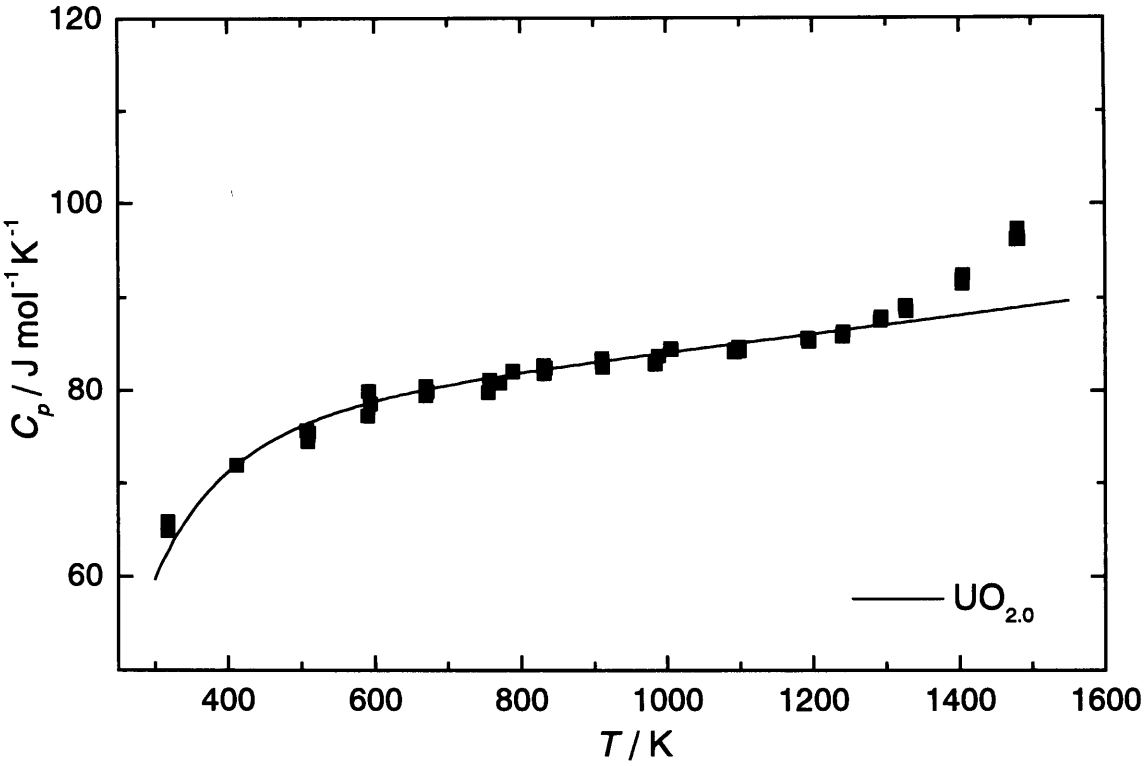

Fig.3-5 Heat capacity of $(U_{0.910}Nd_{0.090})O_{2.0}$.

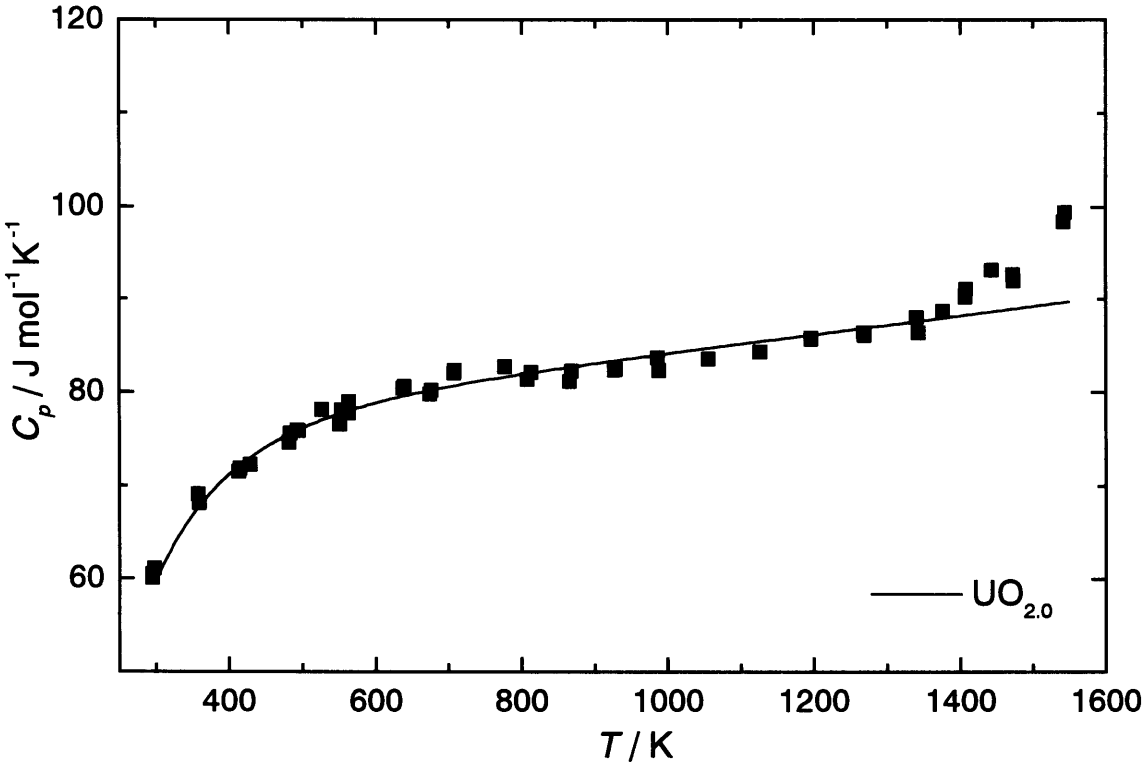

Fig.3-6 Heat capacity of $(U_{0.910}Y_{0.090})O_{2.0}$.

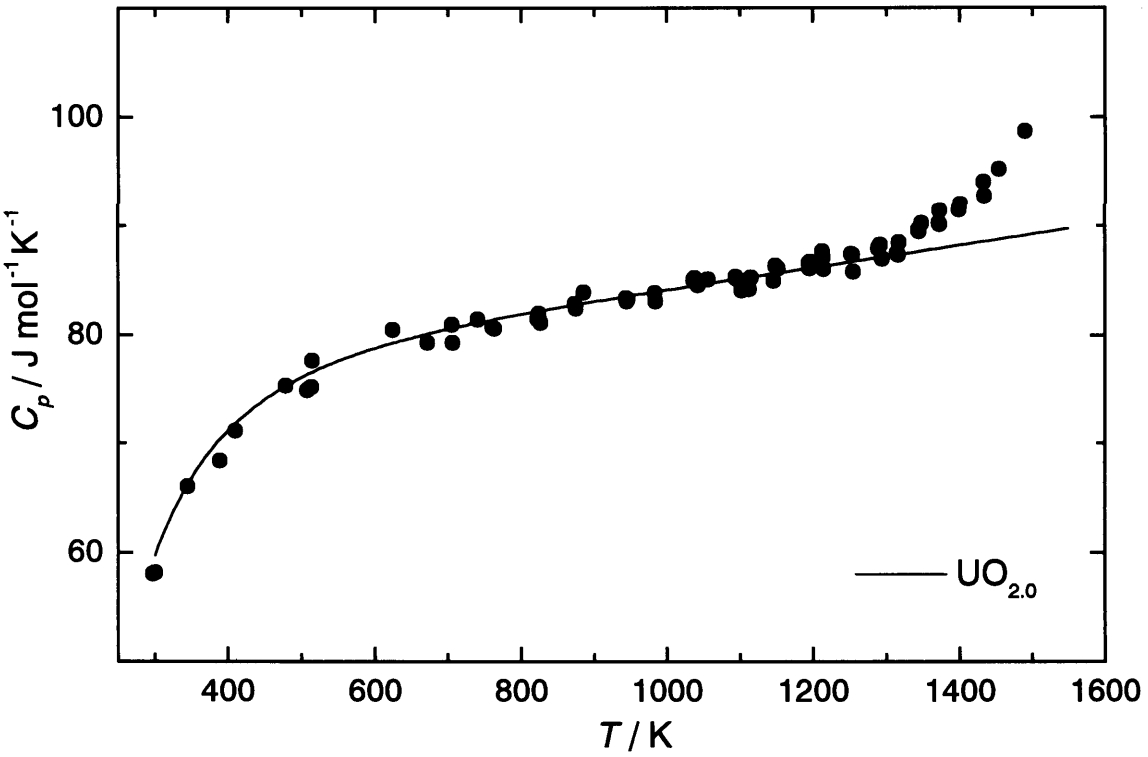

Fig.3-7 Heat capacity of $(U_{0.910}Sc_{0.090})O_{2.0}$.

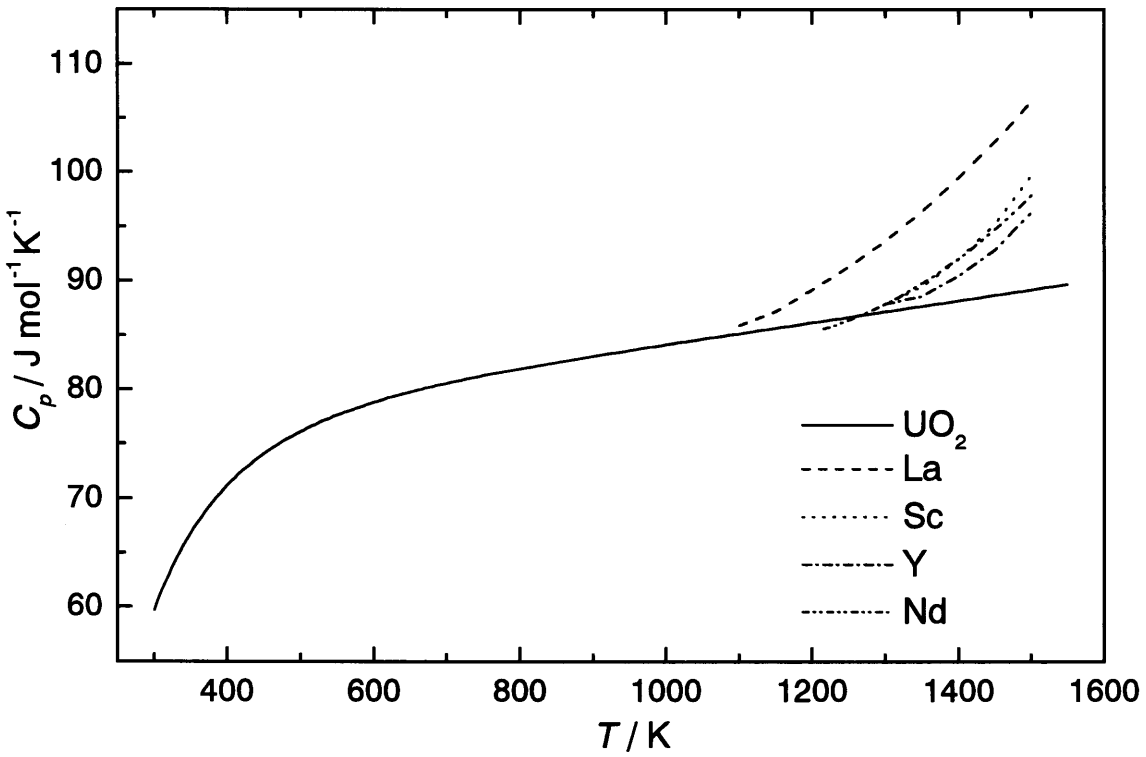

Fig.3-8 Heat capacity of $(U_{0.910}M_{0.090})O_{2.0}$.

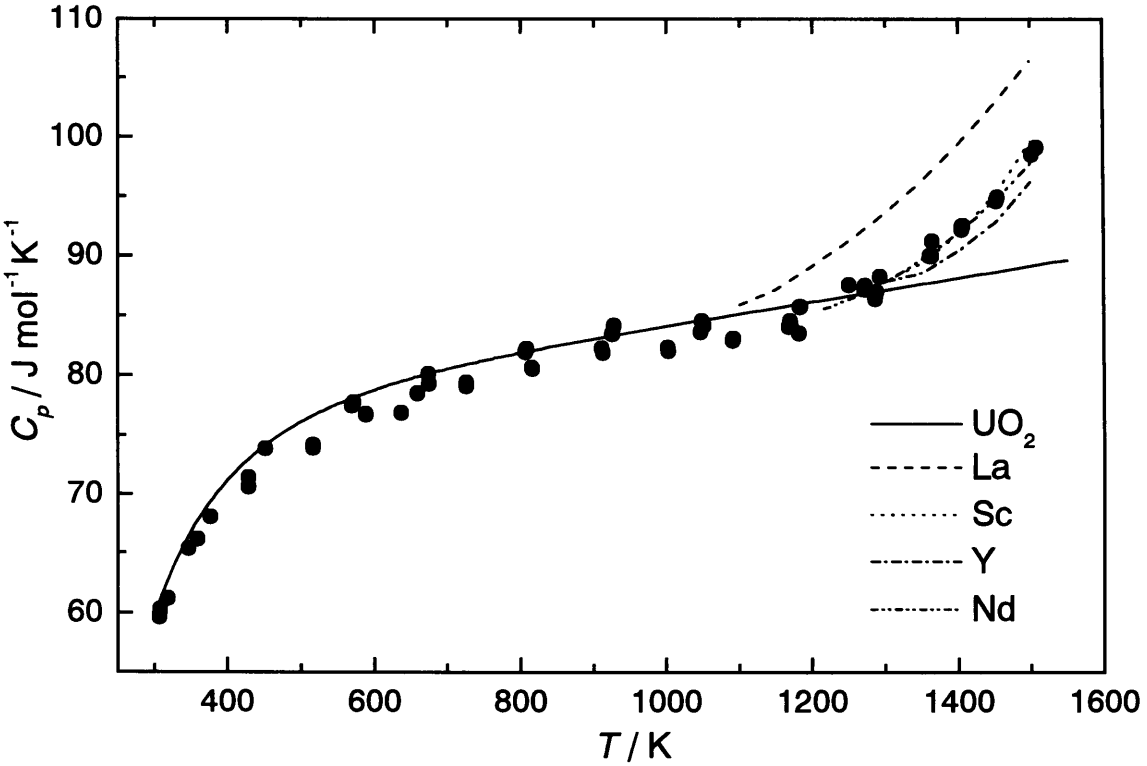

Fig.3-9 Heat capacity of $(U_{0.910}Mg_{0.090})O_{2.0}$.

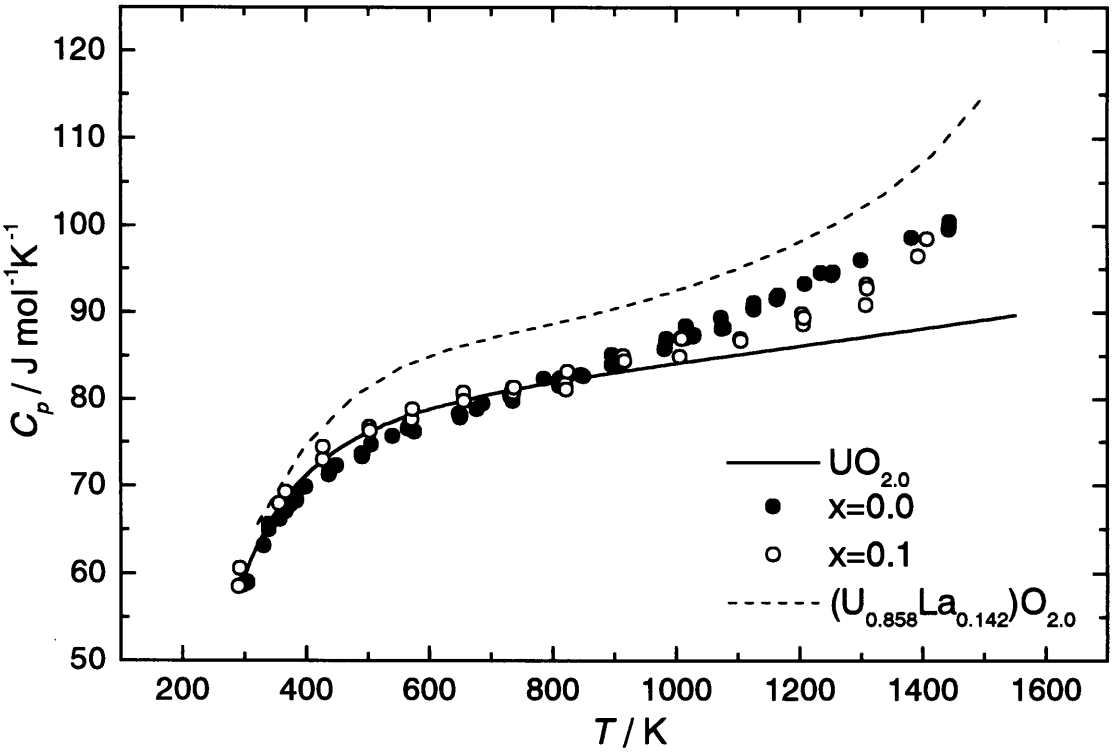

Fig.3-10 Heat capacities of $(U_{0.85}Mg_{0.15})O_{2-x}$.

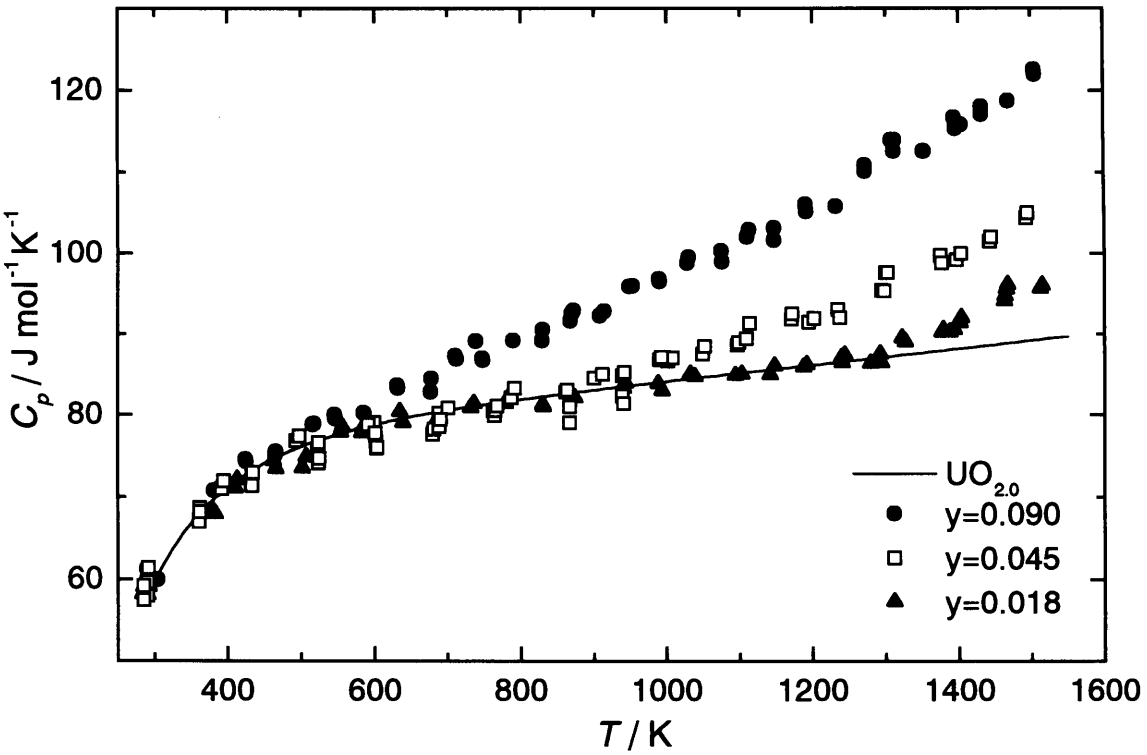

Fig.3-11 Heat capacity of $(U_{1-y}FP_y)O_{2.0}$.

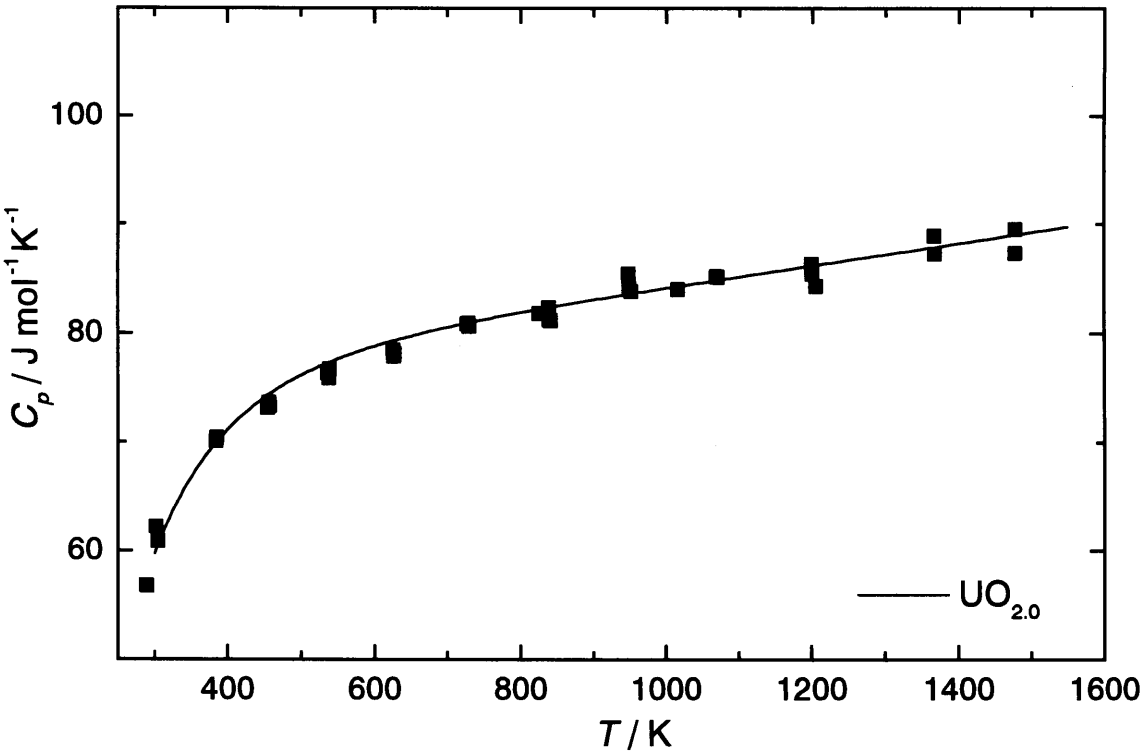

Fig.3-12 Heat capacity of $(U_{0.993}Ti_{0.007})O_{2.0}$.

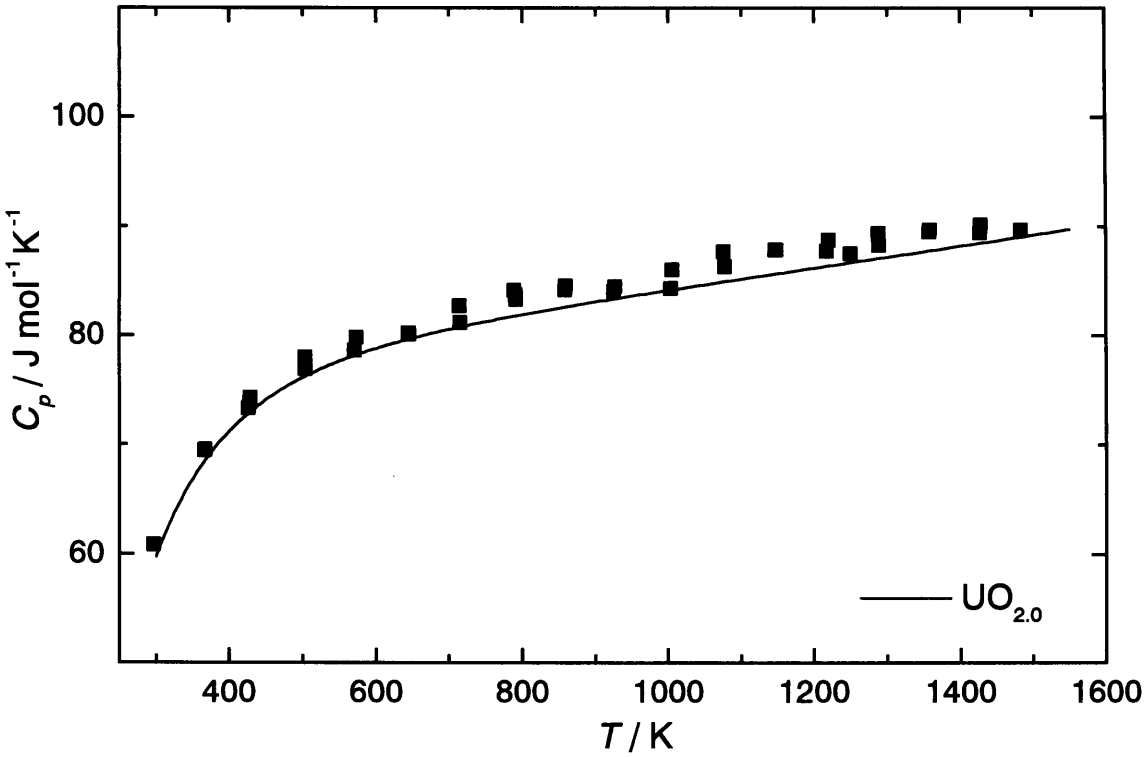

Fig.3-13 Heat capacity of $(U_{0.990}Nb_{0.010})O_{2.0}$.

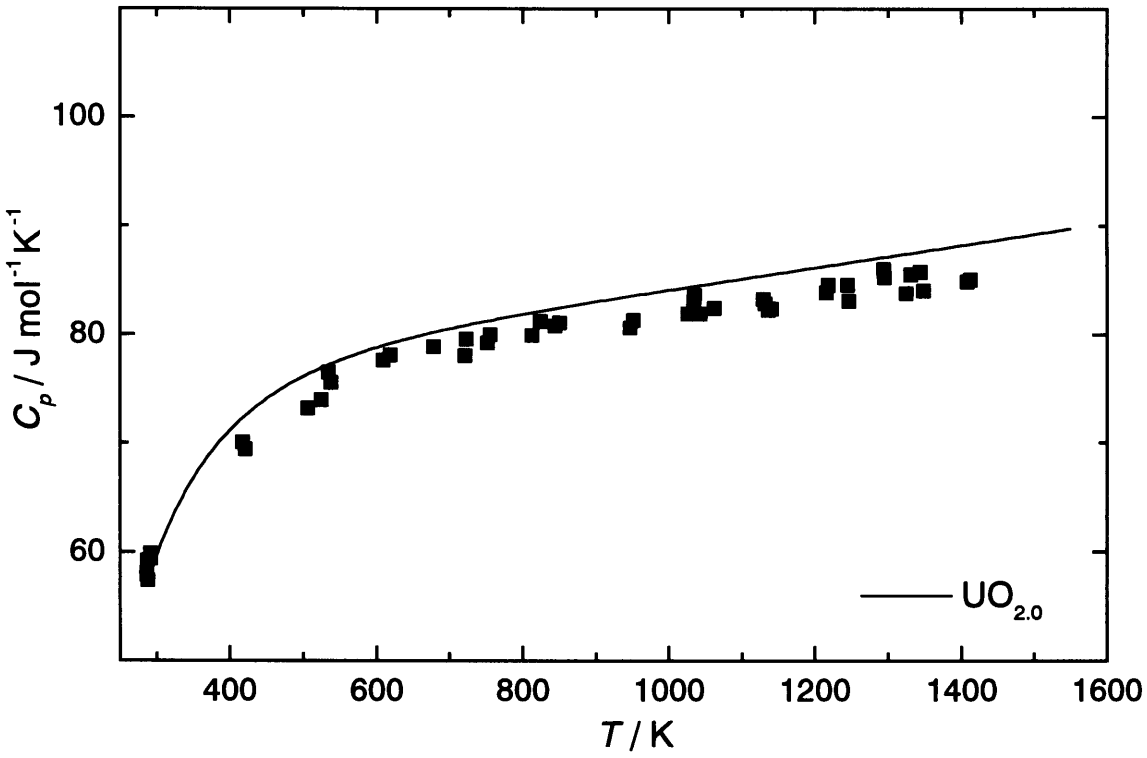

Fig.3-14 Heat capacity of $(U_{0.910}Ce_{0.090})O_{2.0}$.

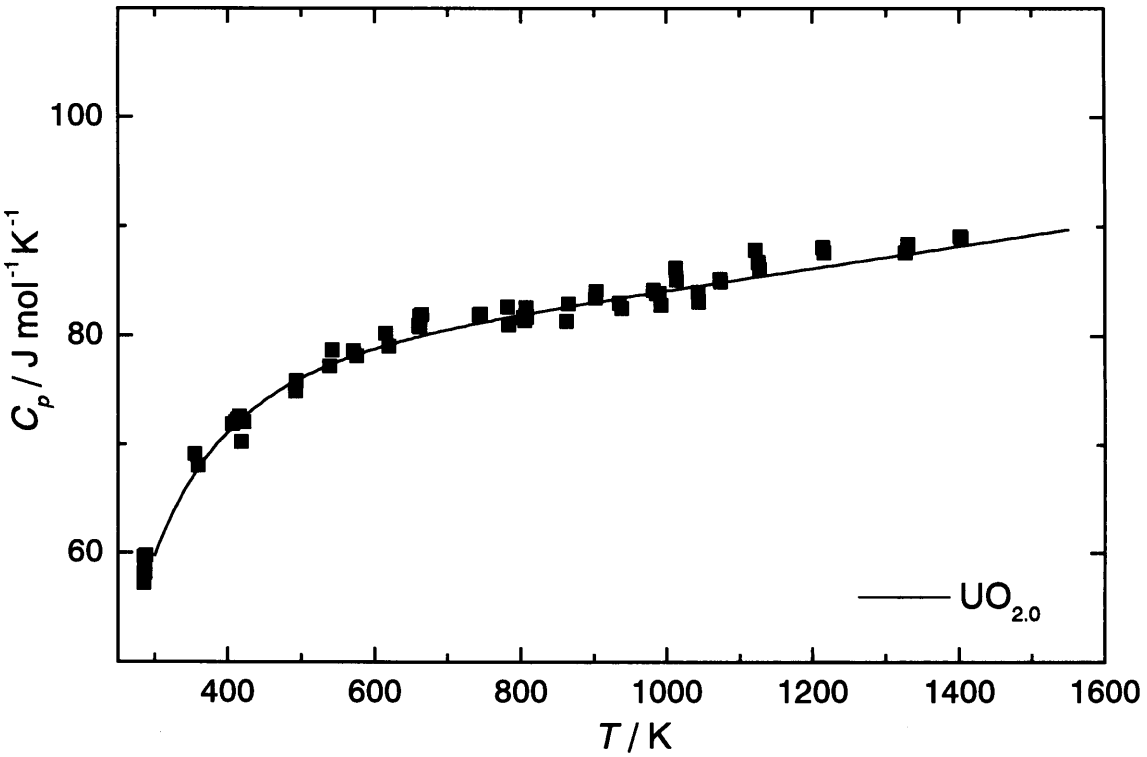

Fig.3-15 Heat capacity of $(U_{0.910}Pr_{0.090})O_{2.0}$.

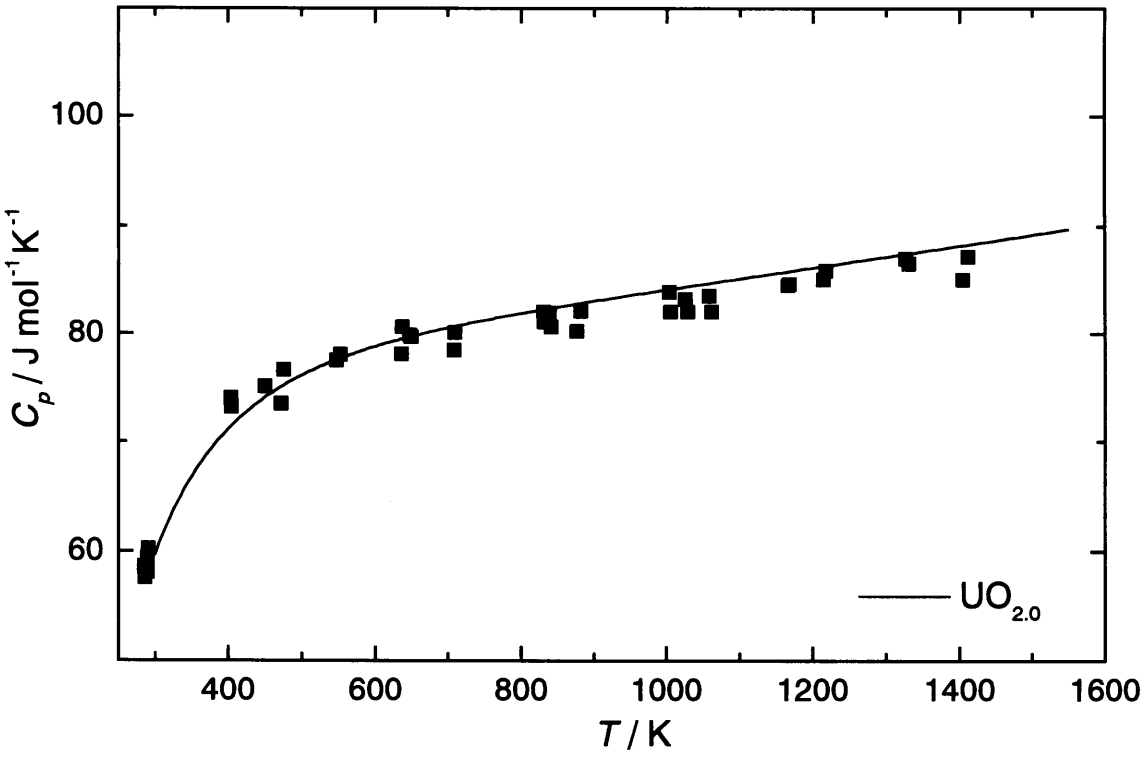

Fig.3-16 Heat capacity of $(U_{0.910}Zr_{0.090})O_{2.0}$.

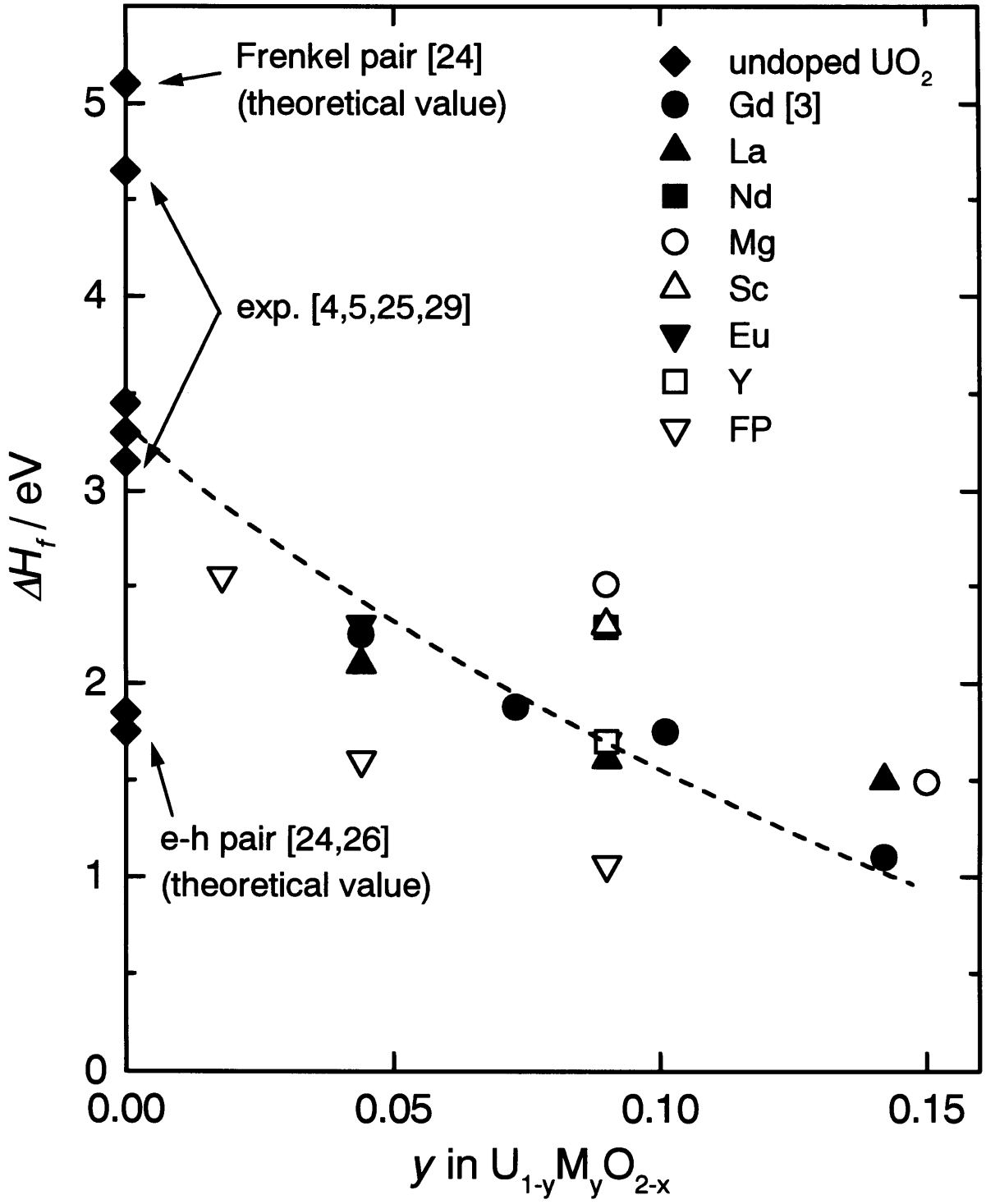

Fig.3-17 Enthalpy of defect formation.

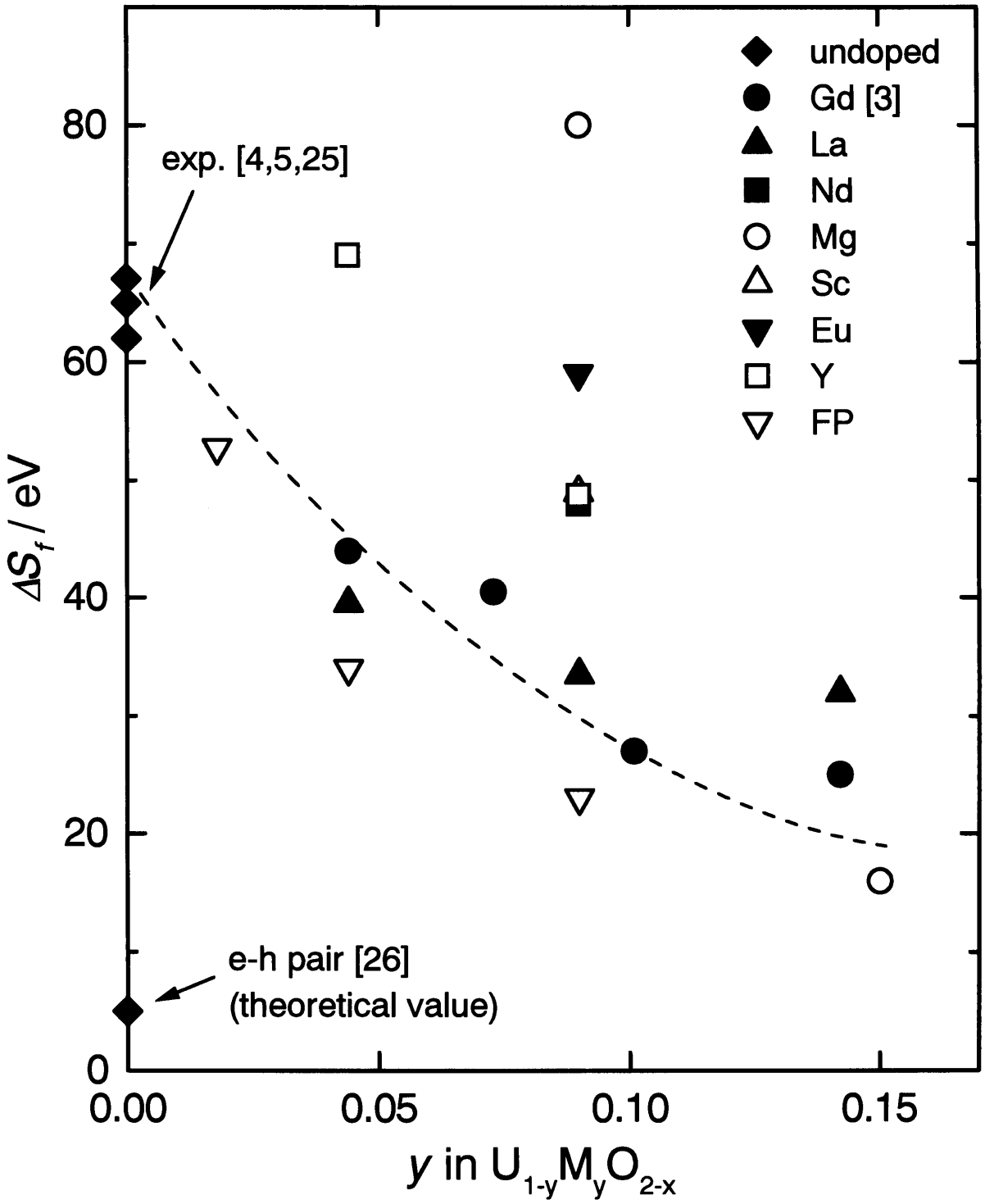

Fig.3-18 Entropy of defect formation.

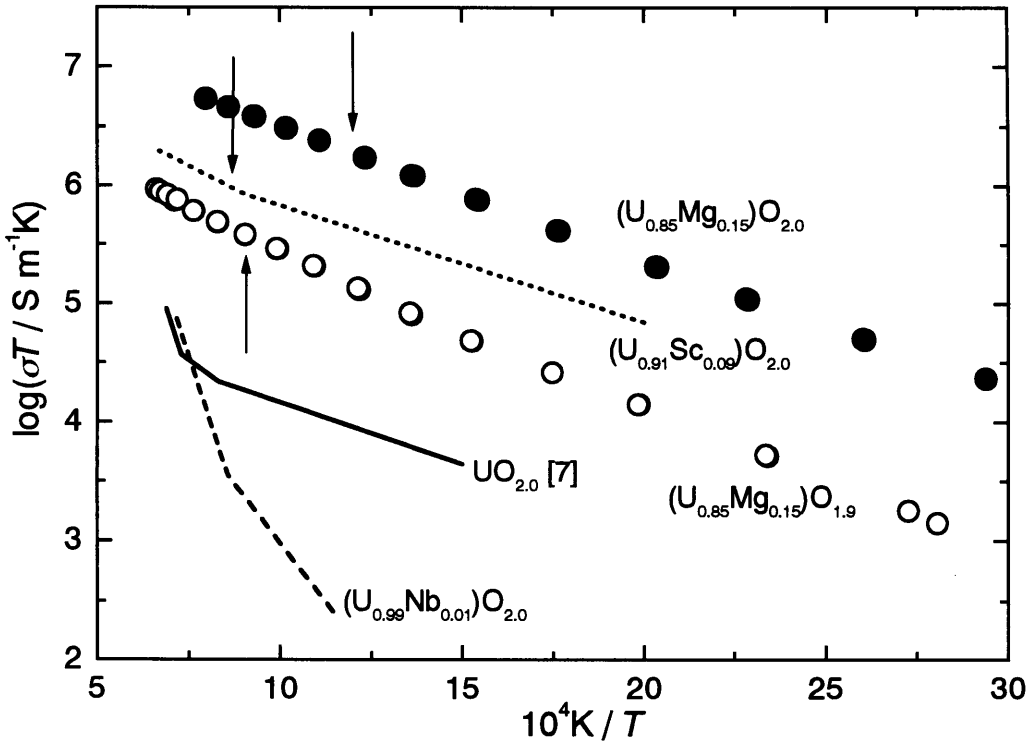

Fig.3-19 Electrical conductivity (allows show T_r).

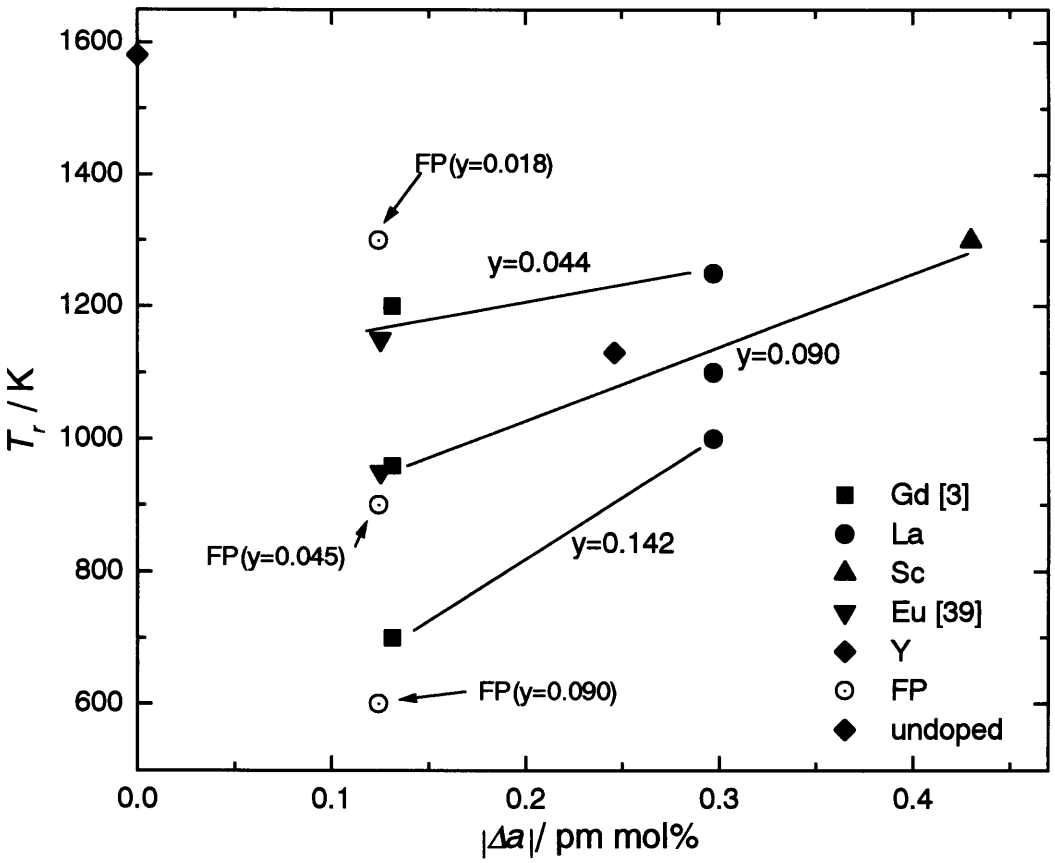

Fig.3-20 Relation between the onset temperature of the heat capacity anomaly and the change in the lattice parameter of $(U_{1-y}M_y)O_2$.

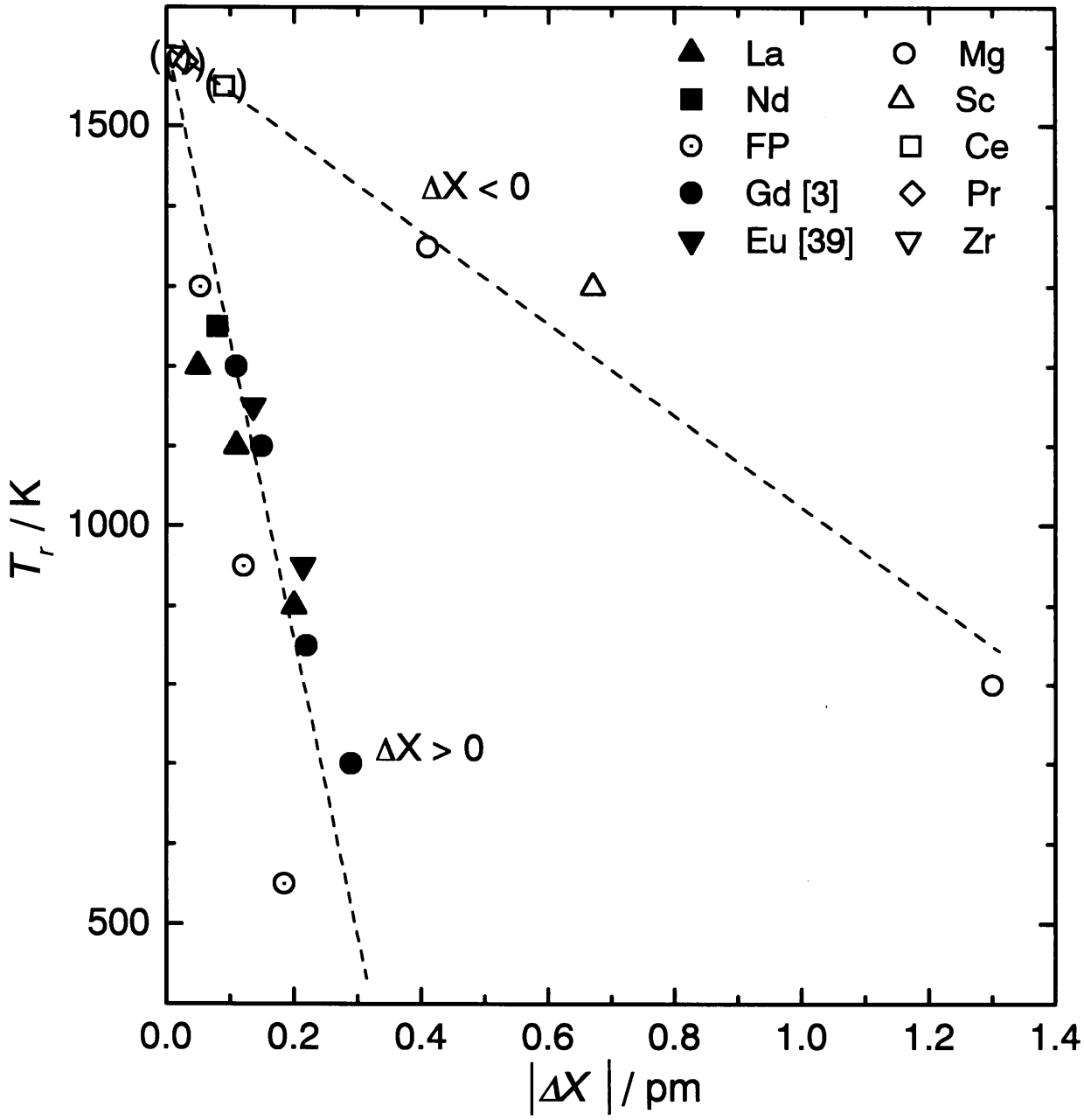

Fig.3-21 Onset temperature as a function of lattice distortion.

4. EXAFS study of doped UO_2

4.1. Introduction

Extended X-ray absorption fine structure (EXAFS) refers to the oscillatory variation of the X-ray absorption as a function of photon energy beyond an absorption edge. The absorption, normally expressed in terms of absorption coefficient (μ), can be determined from a measurement of the intensity attenuation of X-rays upon their passage through a material. When the X-ray photon energy (E) is tuned to the binding energy of some core level of an atom in the material, an abrupt increase in the absorption coefficient, known as the absorption edge, occurs. For isolated atoms the absorption coefficient decreases monotonically as a function of energy beyond the edge. For atoms either in a molecule or embedded in a condensed phase, the variation of absorption coefficient at energies above the absorption edge displays a fine structure called EXAFS. Such fine structure may extend up to 1000 eV above the absorption edge and may have an amplitude of up to a few tenths (normally 1-20 %) of the edge jump.

The recent availability of synchrotron radiation has resulted in the establishment of EXAFS as a practical tool particularly. This technique is especially valuable for structural analyses where conventional diffraction methods are not applicable.

In the case of UO_2 there was no EXAFS studies except those performed by Allen et al. [1-3]. They only examined the oxygen interstitial configuration in U_4O_9 and U_3O_8 [1,2] and the interatomic distances of $(U_{1-y}Ce_y)O_{2-x}$ (y = 0.07, 0.020 and 0.028) [3], however, the detail discussion was not performed.

As discussed in the previous chapter, lattice distortion of the doped UO_2 may be concerned with the origin of the heat capacity anomaly. In this chapter, local structural arrangements of oxygen around the cations in undoped and Mg-doped UO_2 were discussed using data from EXAFS experiment.

4.2. Experimental

4.2.1. EXAFS spectroscopy

EXAFS spectroscopy refers to the measurement of the X-ray absorption coefficient μ as a function of photon energy E above the threshold of an absorption edge. Figure 4-1 shows a schematically one edge of uranium as an absorber. In a transmission experiment as seen from Fig. 4-2, μ or μt (t is the sample thickness) is calculated by :

$$\mu t = \ln(I_0 / I) , \qquad (1)$$

where I_0 and I are the intensities of the incident and transmitted beams, respectively.

EXAFS spectra generally refer to the region 40 - 1000 eV above the absorption edge. Near or below the edge, there generally appear absorption peaks due to excitation of core electrons to some bound states (1*s* to n*d*, (n+1)*s* or (n+1)*p* orbitals for *K*-edge and 2*s* for L_I edge, 2*p* for L_{II} , L_{III} -edges to the same set of vacant orbitals, etc.)[4]. This pre-edge region contains valuable bonding information such as the energetics of virtual orbitals, the electronic configuration and the site symmetry. The edge position also contains information about the charge on the absorber. It arises from effects such as many-body interactions, multiple scatterings, distortion of the exited state wave function by the Coulomb field, band structures, etc.

In this study, EXAFS experiments were carried out at Photon Factory of the National Laboratory for High Energy Physics (KEK-PF, Tsukuba) using the BL—27B line at the uranium L_{III}-edge (17.164 keV) for $UO_{2.0}$, $(U_{0.85}Mg_{0.15})O_{1.9}$ and $(U_{0.85}Mg_{0.15})O_{2.0}$ at room temperature. Unfortunately, EXAFS of magnesium and oxygen could not be obtained at BL-27, since X-ray energies of *K*-edge of magnesium and oxygen are so low (1.3 and 0.53 keV, respectively) that X-ray is mainly absorbed by oxygen and nitrogen on the air pass.

Continuous X-rays from synchrotron radiation are monochromatized by a silicon (111) channel-cut-crystal monochromater. The X-ray beam size is about 1×7 mm^2. X-ray intensities at the front (I_0) and rear (I) of the sample were measured for 1 sec for each of the 500 ~ 600 points from a few tens eV before absorption edge to about

1.0 keV higher in energy.

4.2.2. Sample preparation

X-ray absorption experiments were carried out for the samples prepared in chapter 3. All samples for EXAFS experiments were powder and mixed with boron nitride (BN) powder to reduce the X-ray absorbance. Then the mixed samples were pressed into the pellet of 10 mm $^{\phi}$ and thickness was controlled to be μt = 2~3 at energies slightly higher than the absorption edge.

4.3. Results and discussion

4.3.1. EXAFS spectrum

Absorption spectra near the uranium L_{III}-edge are shown in Fig. 4-3. The EXAFS function χ is typically plotted in terms of the photoelectron wave vector k, where k is related to kinetic energy of the photoelectron (E) by

$$k = 2\pi / h\left[2m(E - E_0)\right]^2 . \qquad (2)$$

E_0 is the threshold energy of the photoelectron at $k = 0$, h is Planck's constant and m is the mass of the electron. In obtaining the EXAFS function $\chi(k)$, the background level was subtracted from the observed absorption coefficient by using a Victreen fit [5] and the absorption coefficient for the isolated atom was obtained by the cubic spline technique. Using a single scattering approximation, the EXAFS for an L_{III} edge is [2]:

$$\chi(k) = \sum_j \frac{N_j \cdot \gamma_j \cdot F_j(k)}{k r_j^2} \exp(-2k^2\sigma_j^2) \cdot \exp(-2r_j / \lambda(k)) \cdot \sin\left[2kR_j + \phi_j(k)\right] , \qquad (3)$$

where N_j is the average number of atoms of a particular element in a shell j at an average radius R_j from the absorbing atom. σ_j is a Debye-Waller like factor which represents the relative root-mean-square displacement from R_j due to thermal (vibrational) and static disorder. λ_j is the mean free path of the electron and γ an amplitude reduction term. The $F_j(k)$ and $\phi_j(k)$ are the backscattering and phase

shift functions, respectively. Fig. 4-4 shows the plots of χk^n vs k (n = 3). The factor k^n, used to weight the data according to the value of k, counteracts the rapid damping of χ with increasing k.

4.3.2. Local structures of Mg-doped UO_{2-X} and undoped $UO_{2.0}$

The Fourier transformation of k^3 gives a "radial structure function" (R.S.F.) of the shells around the atom absorbing X-ray. In this representation, each shell of atoms appears as a peak whose maximum is slightly shifted due to the k dependence of ϕ. The Fourier transformed EXAFS spectra of the $UO_{2.0}$, $(U_{0.85}Mg_{0.15})O_{1.9}$ and $(U_{0.85}Mg_{0.15})O_{2.0}$, measured at the uranium absorption edge, are shown in Fig. 4-5. Two main peaks in the spectra of $UO_{2.0}$ and $(U_{0.85}Mg_{0.15})O_{1.9}$ may be attributed, in order of increasing distance, to the couples of uranium-oxygen and uranium-uranium, and the structure is essentially of a fluorite type. However, in the case of $(U_{0.85}Mg_{0.15})O_{2.0}$, the first peak split into two broad peaks, suggesting the presence of more than two different oxygen shells around the uranium atom.

The treatment of EXAFS data frequently involves the inverse Fourier transform of R.S.F. over a limited range of R. This procedure isolates the contribution to EXAFS arising from shells of atoms within that range of R. The parameters of this equation can then be obtained by a least-squares fitting procedure, provided that the phase [$\phi(k)$] and amplitude [$f(k)$] are known. From a practical viewpoint [$\phi(k)$] and [$f(k)$] have been derived from stoichiometric $UO_{2.0}$. Hence, the results represent the structural deviation from "standard" $UO_{2.0}$. An estimate of an absolute σ, although not essential, has been made in order to allow comparison with *ab initio* values for other atoms.

The separate contributions of the U-O and U-U shells were filtered and inverse Fourier transformation was then fitted to the EXAFS equation using least-squares minimization routines with the reference parameters derived from EXAFS spectra of undoped $UO_{2.0}$.

As seen from Fig. 4-6, all r(U-U) values of $UO_{2.0}$, $(U_{0.85}Mg_{0.15})O_{1.9}$ and $(U_{0.85}Mg_{0.15})O_{2.0}$ from EXAFS are almost the same as those calculated theoretically

from lattice constants. On the other hand, r(U-O) values of $(U_{0.85}Mg_{0.15})O_{2.0}$ from EXAFS are not equal to a value estimated from the lattice constant, but seems to be split into two different distances. Although r(U-O) value is regarded to have more than two different distances, the interatomic distances were calculated on the assumption that there are two U-O shells. To make clear the variety of the U-O shell, the theoretical calculation of R.S.F. is in preparation.

In fluorite structure, cation has eight oxygens as the nearest neighbor atoms. Table 4-1 gives the fitted value of the coordination number for the nearest-neighbor oxygen shell of the uranium atom.

Table 4-1 Interatomic distance (R), coordination number of oxygen around uranium (N) and temperature of heat capacity increase anomaly

Sample	*r(U-O)* *(nm)*	*N*	T_r *(K)*
$UO_{2.0}$	0.237	8.0	1600
$(U_{0.85}Mg_{0.15})O_{1.9}$	0.236	8.5	1150
$(U_{0.85}Mg_{0.15})O_{2.0}$	0.213 ~0.246	~10.5	800

The local structural environments of Y^{3+} and Zr^{4+} ions in 18 wt% Y_2O_3 doped ZrO_2 were previously studied by using EXAFS spectroscopy over the temperature range from 153 to 1043 K [6]. The oxygen arrangements around Y^{3+} and Zr^{4+} were found to be different from each other i.e. more oxygen vacancies were sited adjacent to Zr^{4+} and were more disordered than those near Y^{3+} at low temperature. The structural environment of Zr^{4+} in cubic ZrO_2 resembled that of the 7-coordinated Zr^{4+} in monoclinic ZrO_2. As seen from Fig. 4-7, the temperature rise of the sample resulted in the local structural environments of two cations becoming more alike. It suggests that increase in the oxygen mobility enhances randomness in the spatial distribution of

oxygen defects.

In the case of $UO_{2.0}$, uranium has eighthold coordination of oxygen, but both in $(U_{0.85}Mg_{0.15})O_{1.9}$ and $(U_{0.85}Mg_{0.15})O_{2.0}$, the coordination numbers are larger than eight. It suggests that oxygen atom is more favorable around uranium atom than magnesium atom. Furthermore, in the case of $(U_{0.85}Mg_{0.15})O_{2.0}$, oxygen environment around the cations including oxygen vacancies around magnesium atom, is considered to be disordered i.e. non-uniform. Therefore oxygen Frenkel defects are preferably formed with increasing temperature such as to make the distribution of oxygen defects around magnesium and uranium uniform (disordered), resulting in the heat capacity anomaly, consisting to the smaller enthalpy of formation of oxygen Frenkel defect for $(U_{0.85}Mg_{0.15})O_{2.0}$ compared to $(U_{0.85}Mg_{0.15})O_{1.9}$.

The information of the temperature dependence of interatomic distances for uranium-oxygen and uranium-cations is necessary for more detailed discussion. Now we are constructing the apparatus of the high temperature EXAFS study for radioactive materials. (Fig. 4-8).

4.4. Conclusions

The conclusions obtained in this chapter are summarized here :

By EXAFS experiments, it was found that the environment of oxygen and oxygen vacancy around the cations is considered to be disordered for $(U_{0.85}Mg_{0.15})O_{2.0}$. Oxygen exists preferably around uranium. Oxygen vacancy, by contrast, is more favorable around magnesium. Therefore formation of oxygen Frenkel defects are enhanced at elevated temperature such as to make the distribution of oxygen defects around magnesium and uranium uniform (disordered), resulting in the heat capacity anomaly, consisting to the smaller enthalpy of formation of oxygen Frenkel defect for $(U_{0.85}Mg_{0.15})O_{2.0}$ compared to $(U_{0.85}Mg_{0.15})O_{1.9}$.

References

[1] G.C.Allen, P.A.Tempest, C.D.Garner, I.Ross and D.J.Jones, *J. Phys. Chem.*, **89** (1985) 1334.

[2] D.J.Jones, J.Roziere, G.C.Allen and P.A.Tempest, *J. Chem. Phys.*, **84** (1986) 6075.

[3] D.J.Jones, J.Roziere, G.C.Allen and P.A.Tempest, *J. de Phys.*, **47** (1986) C8-745.

[4] B.K.Teo, "EXAFS : Basic Principles and Data Analysis", (Springer-Verlag, Berlin, 1985) p.21.

[5] J.A.Victoreen, *J. Appl. Phys.*, **19** (1948) 855.

[6] C.R.A.Catlow, A.V.Chadwick, G.N.Greaves and L.M.Moroney, *J. Am. Ceram. Soc.*, **69** (1986) 272.

[7] T.Matsui, H.Yokoi, Y.Arita, H.Ohno and K.Kobayashi, *Photon Factory Activity Rep.*, **12** (1994) 111.

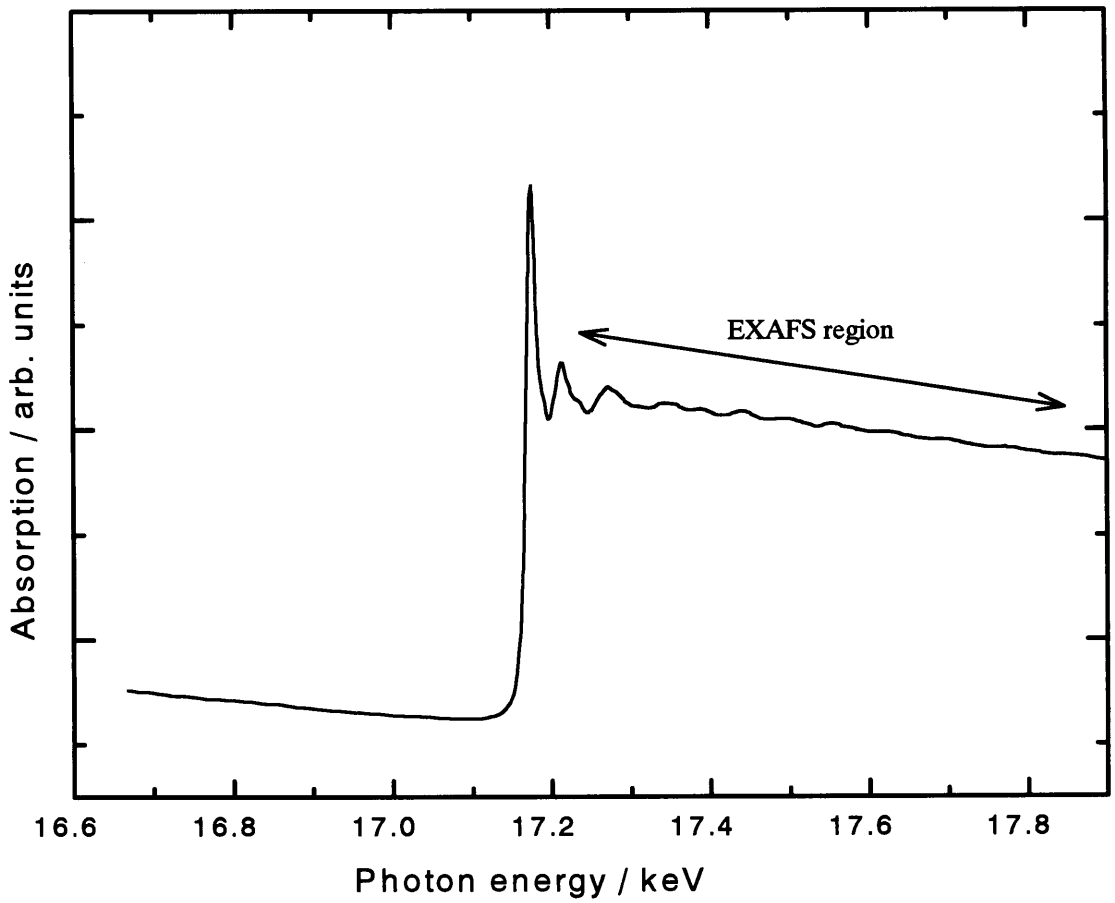

Fig.4-1 X-ray absorption spectrum of U-L_{III} edge.

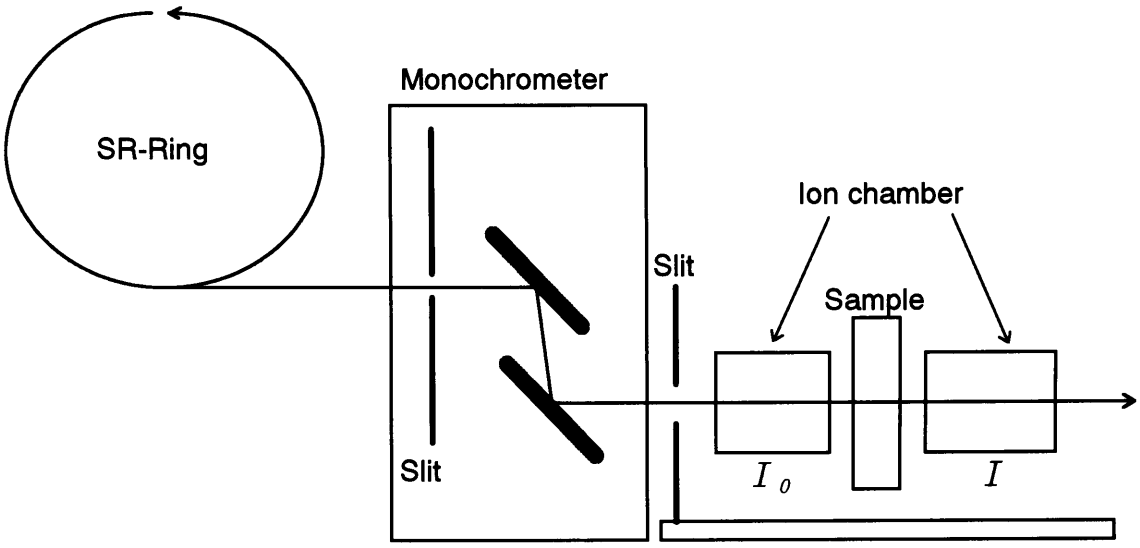

Fig.4-2 The configuration of the apparatus of transmission method.

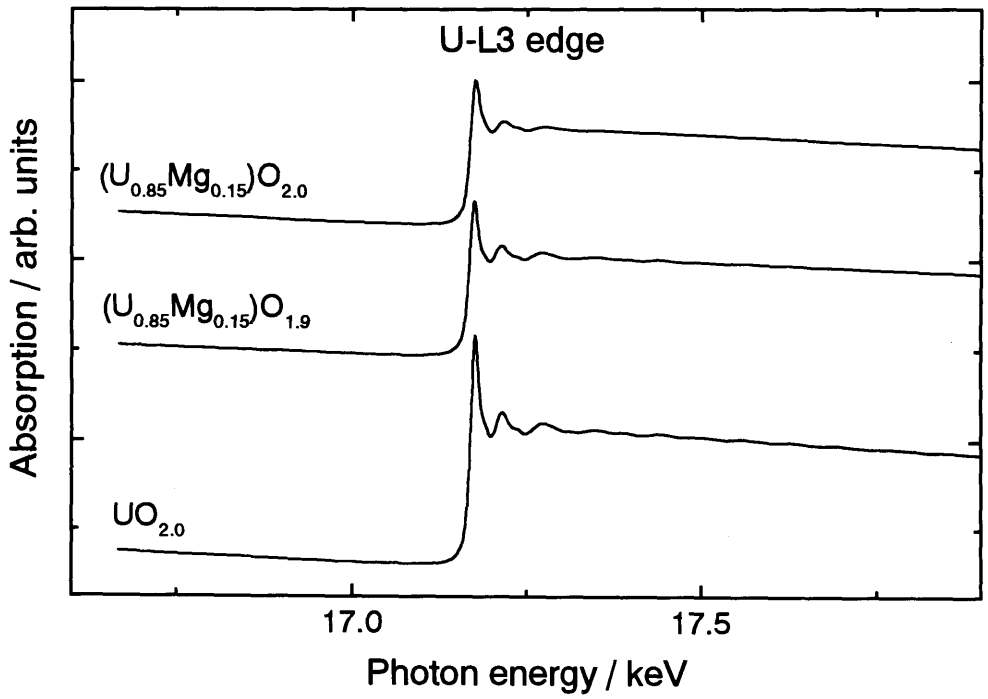

Fig.4-3 X-ray absorption spectrum.

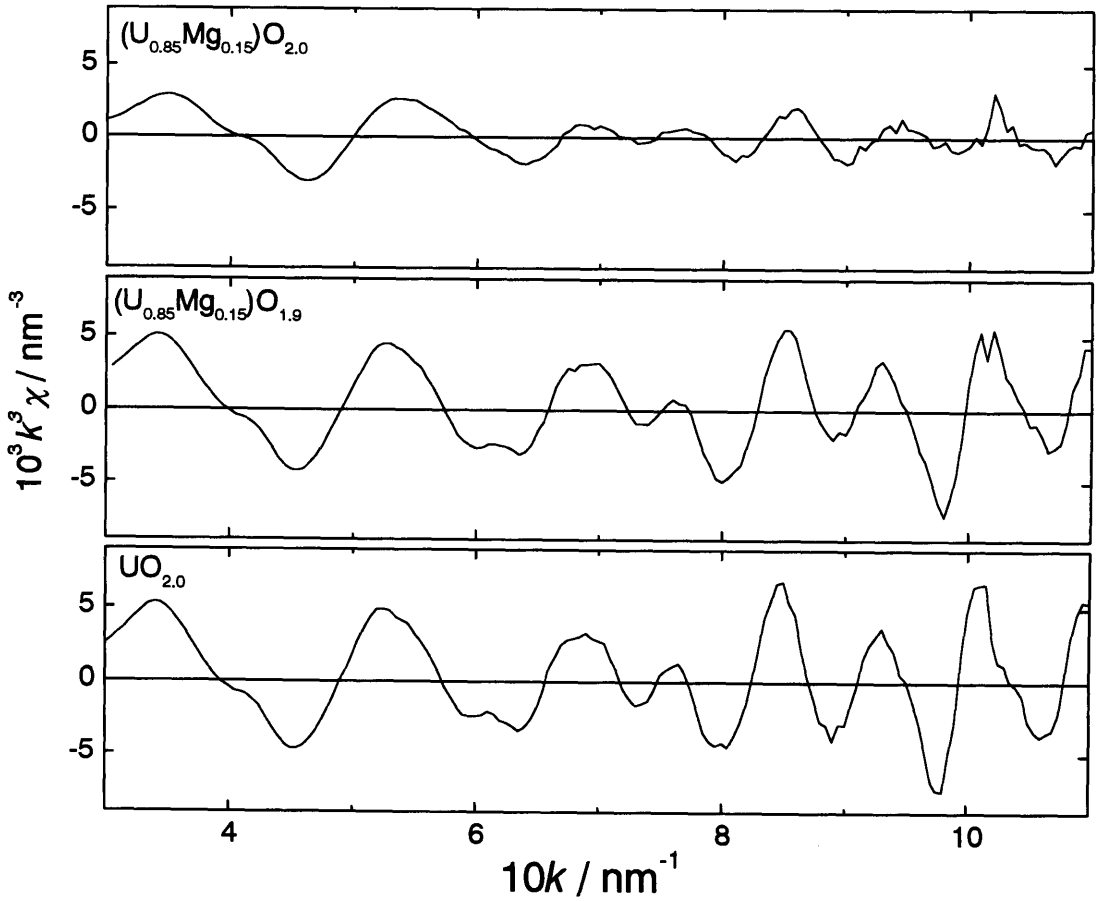

Fig.4-4 The k^3-weighted EXAFS curve.

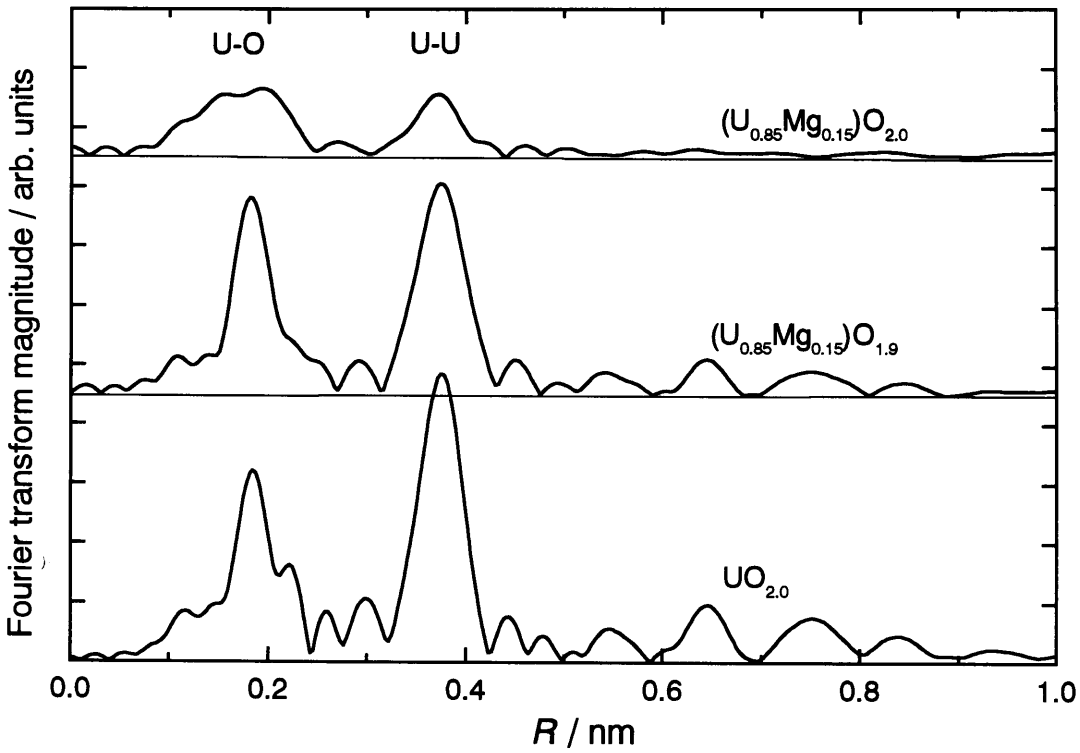

Fig.4-5 Radial structure functions.

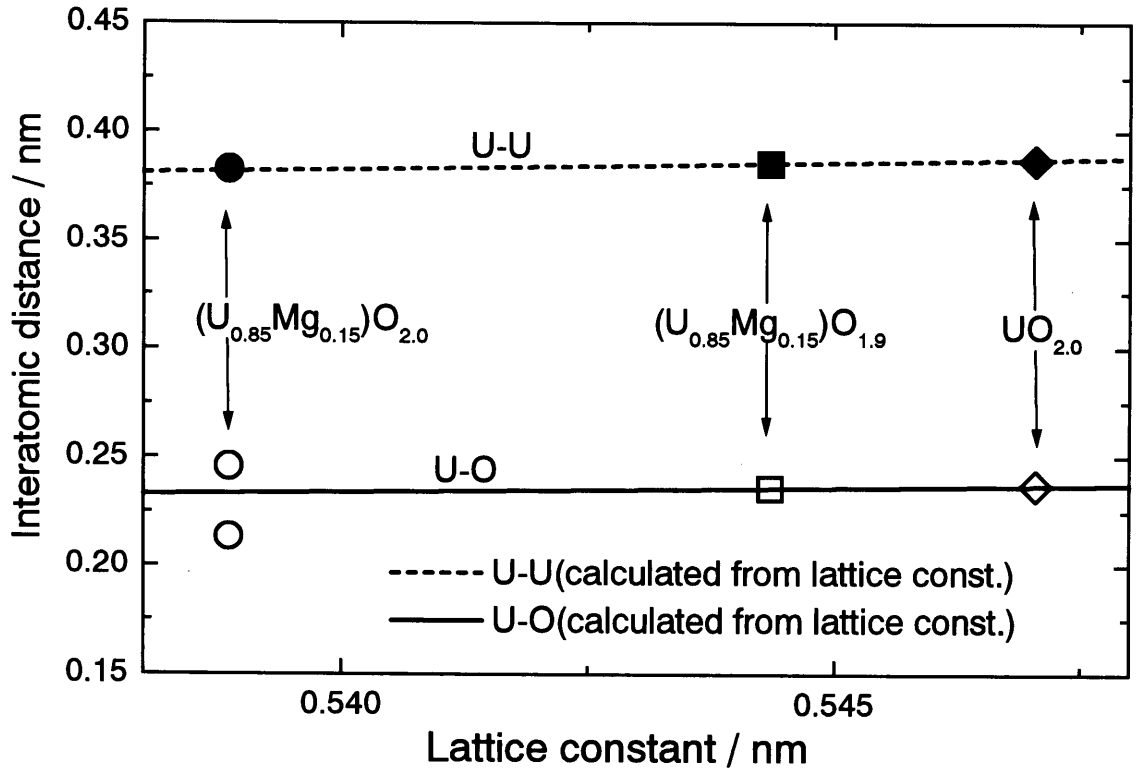

Fig.4-6 Interatomic distances from EXAFS result.

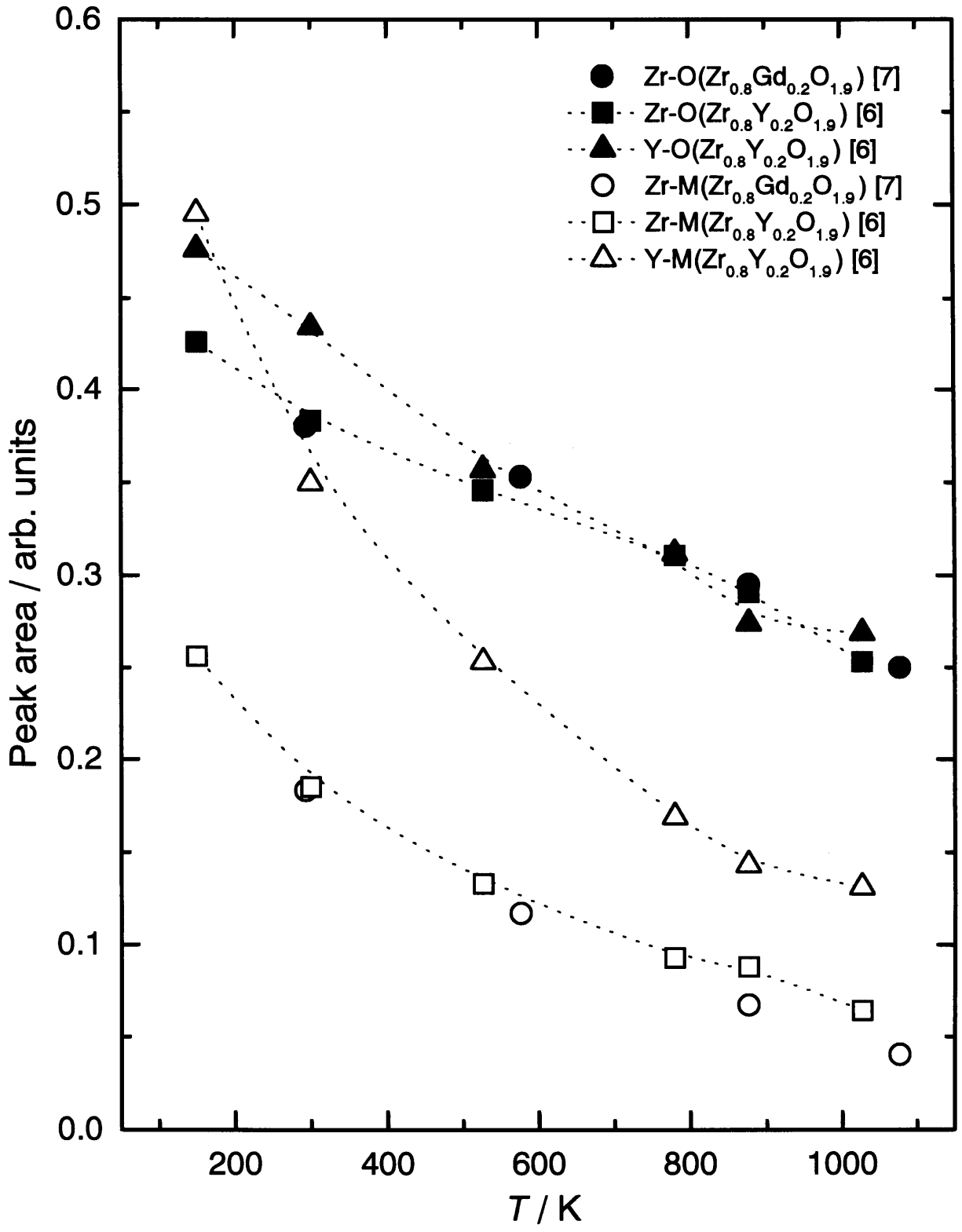

Fig.4-7 Variation with temperature of the areas of Zr-O, Y-O, Zr-M and Y-M peaks in magnitude of Fourier-transformed EXAFS data.

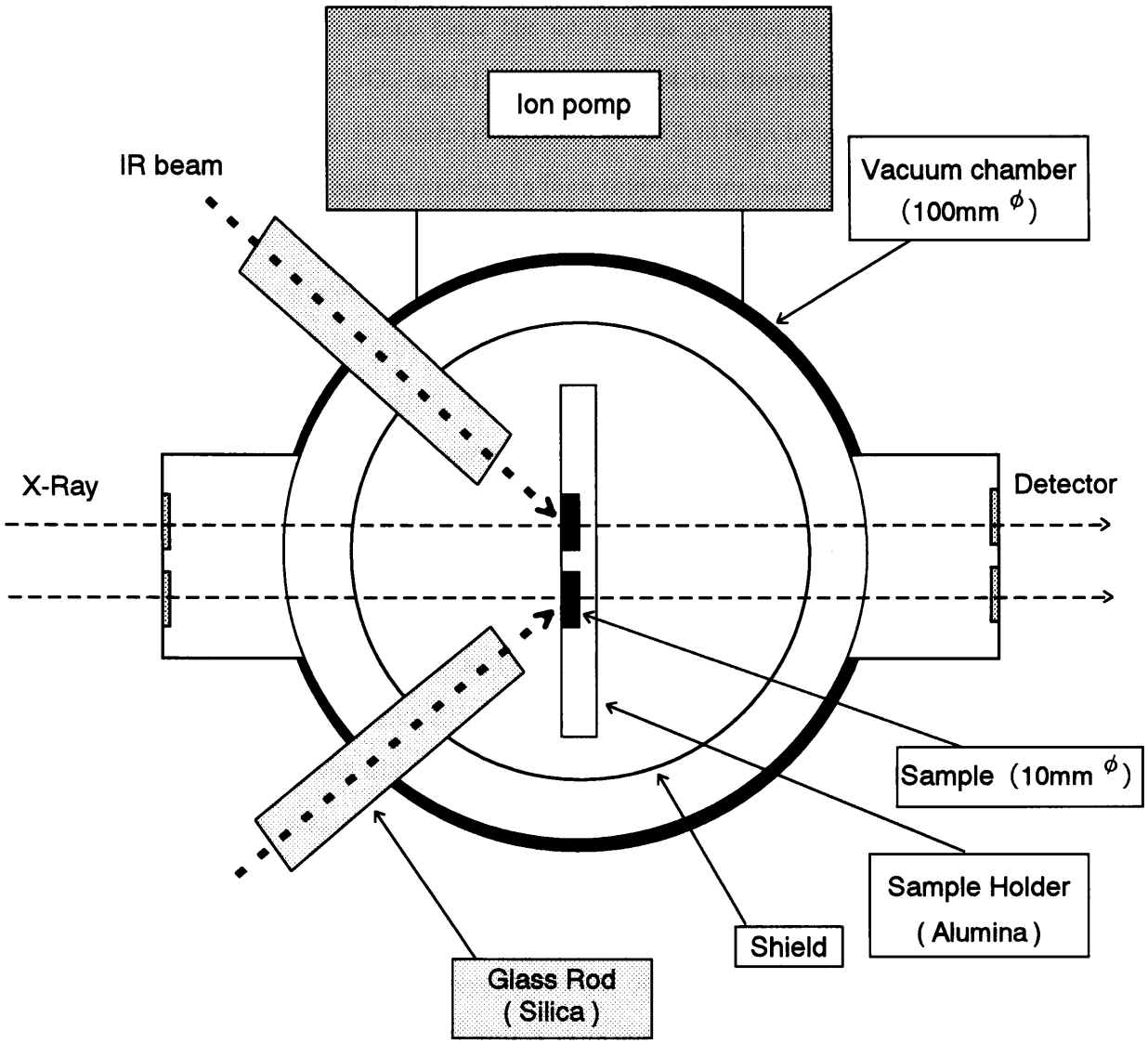

Fig4-8 Top view of the high temperature EXAFS apparatus.

5. Conclusions

In this thesis the high temperature heat capacities of UO_2 doped with various cations were measured to make clear the anomalous increase in the heat capacity of undoped UO_2 and doped UO_2, and I have calculated the thermal functions which are useful quantities to provide the thermal behavior of UO_2 at high temperature.

In chapter 1, the previous studies on high temperature heat capacity and origins of the excess heat capacity of undoped UO_2 were introduced. It was pointed out that the excess heat capacity of undoped seemed to be originated by the oxygen Frenkel defects or electron-hole pairs. The purpose of this work was described.

In chapter 2, I summarized that the improvements of the direct heating pulse calorimeter were performed to measure the heat capacity at higher temperature range and more conveniently. By the improvements, the measurable temperature for regular usage and maximum became 1550 K and 1783 K, respectively. Further the DHPC was improved to be useful for the high resistant sample.

In chapter 3, the heat capacities of the UO_2 doped with various cations (La, Nd, Y, Sc, FP, Mg, Ti, Nb, Ce, Pr and Zr) were measured and the origin of the excess heat capacity of doped UO_2 was discussed in comparison with those of undoped UO_2. The excess heat capacity was observed in the heat capacity of UO_2 doped with rare-earth, magnesium and simulated fission products, while it was not observed in that doped with tetra- or penta-valent cations. The origin of excess heat capacity of doped and undoped UO_2 was ascribed to formation of oxygen Frenkel defect. The onset temperature which is dependent on thermally activated defect concentration was shown to have relations with the valence, the ionic radius and the concentration of the dopants. The thermal functions for each solid solution were calculated from heat capacity.

In chapter 4, the extended X-ray absorption fine structure experiments of $UO_{2.0}$, $(U_{0.85}Mg_{0.15})O_{2.0}$ and $(U_{0.85}Mg_{0.15})O_{1.9}$ were performed to examine the oxygen configurations around uranium and dopant cation. Oxygen atom is more favorable around uranium atom than magnesium atom and oxygen environment around uranium was shown to be more disordered than that around magnesium in the case of

$(U_{0.85}Mg_{0.15})O_{2.0}$. Therefore, oxygen Frenkel defects are preferably formed with increasing temperature such as to make the distribution of oxygen defects around Mg and U uniform (disordered), resulting in the heat capacity anomaly, consisting to the smaller enthalpy of formation of oxygen Frenkel defect for $(U_{0.85}Mg_{0.15})O_{2.0}$ compared to $(U_{0.85}Mg_{0.15})O_{1.9}$.

Consequently the heat capacity anomalies for UO_2 doped with various cations (La, Nd, Y, Sc, FP, Mg, Ti, Nb, Ce, Pr and Zr) are concluded to originate from oxygen Frenkel pair-like defects and the onset temperatures are concluded to be subject to the oxygen environment around the uranium atom, i.e. the uranium-oxygen interatomic distance and oxygen coordination.

Acknowledgment

The present thesis is the collection of studies which have been carried out under the direction of Emeritus Prof. Keiji NAITO of Department of Nuclear Engineering, Faculty of Engineering, Nagoya University and Prof. Tsuneo MATSUI of Department of Quantum (and Nuclear) Engineering, Graduate School of Engineering, Nagoya University. The author expresses grateful acknowledgment to Dr. Keiji NAITO, Prof. Tsuneo MATSUI and Assoc. Prof. Takanori NAGASAKI for their valuable suggestion, discussion and continuous encouragement throughout this work.

The thesis was completed through the discussions and suggestions by Prof. Tsuneo MATSUI, Prof. Ichiro YAMAMOTO, Prof. Kenji MORITA, Prof. Toshihide TSUJI and Prof. Tetsuo TANABE. I would like to express my thanks to them.

The auther is deeply indebted to Assoc. Prof. Katsumi KOBAYASHI and Dr. Noriko USAMI of Photon Factory, National Laboratory for High Eenrgy Physics (KEK - PF) and Dr. Haruhiko MOTOHASHI and Dr. Hideo OHNO of Japan Atomic Energy Research Institute (JAERI) for the kind support for EXAFS experiments.

Grateful acknowledgment is made to Mr. Nobuyoshi MIYAJIMA, Mr. Seiichi HAMADA, Mr. Hiroto YOKOI and Mr. Tatsuya TOKUNAGA for their continuous assistance in various atages of his work.

The EXAFS experiment of this work has been performed under the approval of the Photon Factory Program Advisory Committee (Proposal No. 93G192 and 95G233) and the program of JAERI-University Research Cooperation.

Finally the author express his gratitude heartly to his parents, Mr. Tamotsu ARITA and Mrs. Toshiko ARITA.

Jan, 1997

Yuji ARITA

List of published papers

(1) T.Matsui, Y.Arita and K.Naito,:

"Heat capacity measurement of $U_{1-y}La_yO_2$ (y = 0.044, 0.090, 0.142) from 300 to 1500K", *J. Radioanal. and Nucl. Chem.*, **43** (1990) 149-156.

(2) T.Matsui, Y.Arita and K.Naito,:

"High temperature heat capacities and electrical conductivities of UO_2 doped with Ti, Nb and Sc", *Solid State Ionics*, **49** (1991) 195-200.

(3) T.Matsui, Y.Arita and K.Naito,:

"High temperature heat capacities and electrical conductivities of UO_2 doped with yttrium and simulated fission products", *J. Nucl. Mater.*, **188** (1992) 205-209.

(4) Y.Arita, S.Hamada and T.Matsui,:

"High temperature heat capacities and electrical conductivities of UO_2 doped with simulated fission products for 2 - 10 at% burnup", *Thermochim. Acta*, **247** (1994) 225-236.

(5) Y.Arita, T.Matsui and S.Hamada,:

"High temperature heat capacities of $U_{0.91}La_{0.09}O_2$ (where M is Pr, Ce, Zr) from 290 to 1410 K", *Thermochim. Acta*, **253** (1995) 1-9.

(6) Y.Arita and T.Matsui,:

"High temperature heat capacities and electrical conductivities of UO_2 doped with Nd and Mg", *Thermochim. Acta*, **267** (1995) 389-396.

(7) Y.Arita, T.Matsui, H.Ohno and K.Kobayashi,:

"Heat capacity measurement and EXAFS study of $(U_{0.85}Mg_{0.15})O_{2-X}$ (x = 0 and 0.1)", *Int. J. Thermophys.*, in print (1996).

(8) T.Matsui, T.Nagasaki, Y.Arita, H.Shigematsu, T.Harami, H.Ohno and K.Kobayashi,: "Application of synchrotron radiation to analysis of local structures in energy-related materials", *J. Nucl. Mater.*, submitted (1996).